

















FAST drift scan survey for H_I intensity mapping: I. preliminary data analysis

YICHAO LI ¹, YOUNGANG WANG ^{2,3,4}, FUREN DENG ^{2,3,4}, WENXIU YANG ^{2,3,4}, WENKAI HU ^{5,6}, DIYANG LIU ¹,
XINYANG ZHAO ¹, SHIFAN ZUO ^{2,4}, SHUANGHAO SHU ^{2,3}, JIXIA LI ^{2,4}, PETER TIMBIE ⁷, RÉZA ANSARI,⁸ OLIVIER PERDEREAU,⁹
ALBERT STEBBINS ¹⁰, LAURA WOLZ ¹¹, FENGQUAN WU ^{2,3,4}, XIN ZHANG ^{1,12,13} AND XUELEI CHEN ^{2,1,4,3}

¹Key Laboratory of Cosmology and Astrophysics (Liaoning) & College of Sciences, Northeastern University, Shenyang 110819, China

²National Astronomical Observatories, Chinese Academy of Sciences, Beijing 100101, China

³School of Astronomy and Space Science, University of Chinese Academy of Sciences, Beijing 100049, China

⁴Key Laboratory of Radio Astronomy and Technology, Chinese Academy of Sciences, A20 Datun Road, Chaoyang District, Beijing 100101, China

⁵Aix Marseille Univ, CNRS, CNES, LAM, Marseille, France

⁶ARC Centre of Excellence for All Sky Astrophysics in 3 Dimensions (ASTRO 3D), Australia

⁷Department of Physics, University of Wisconsin – Madison, Madison, Wisconsin 53706, USA

⁸Université Paris-Saclay, Université Paris Cité, CEA, CNRS, AIM, 91191, Gif-sur-Yvette, France

⁹Université Paris-Saclay, CNRS/IN2P3, IJCLab, 91405 Orsay, France

¹⁰Fermi National Accelerator Laboratory, P.O. Box 500, Batavia IL 60510, USA

¹¹Jodrell Bank Centre for Astrophysics, Department of Physics & Astronomy, The University of Manchester, Manchester M13 9PL, UK

¹²National Frontiers Science Center for Industrial Intelligence and Systems Optimization, Northeastern University, Shenyang 110819, China

¹³Key Laboratory of Data Analytics and Optimization for Smart Industry (Ministry of Education), Northeastern University, Shenyang 110819, China

ABSTRACT

This work presents the initial results of the drift-scan observation for the neutral hydrogen (H_I) intensity mapping survey with the Five-hundred-meter Aperture Spherical radio Telescope (FAST). The data analyzed in this work were collected in night observations from 2019 through 2021. The primary findings are based on 28 hours of drift-scan observation carried out over seven nights in 2021, which covers 60 deg² sky area. Our main findings are: (i) Our calibration strategy can successfully correct both the temporal and bandpass gain variation over the 4-hour drift-scan observation. (ii) The continuum maps of the surveyed region are made with frequency resolution of 28 kHz and pixel area of 2.95 arcmin². The pixel noise levels of the continuum maps are slightly higher than the forecast assuming $T_{\text{sys}} = 20$ K, which are 36.0 mK (for 10.0 s integration time) at the 1050–1150 MHz band, and 25.9 mK (for 16.7 s integration time) at the 1323–1450 MHz band, respectively. (iii) The flux-weighted differential number count is consistent with the NRAO-VLA Sky Survey (NVSS) catalog down to the confusion limit ~ 7 mJy/beam⁻¹. (iv) The continuum flux measurements of the sources are consistent with that found in the literature. The difference in the flux measurement of 81 isolated NVSS sources is about 6.3%. Our research offers a systematic analysis for the FAST H_I intensity mapping drift-scan survey and serves as a helpful resource for further cosmology and associated galaxies sciences with the FAST drift-scan survey.

Keywords: cosmology: large-scale structure of universe — methods: data analysis — surveys

1. INTRODUCTION

Measurements of the cosmological large-scale structure (LSS) play an important role in studying the evolution of the Universe. In the past decades, the LSS fluctuations have been explored by observing the galaxy distribution in the Universe with wide-field spectroscopic and photometric surveys (Cole et al. 2005; Eisenstein et al. 2005; Anderson et al. 2014; Hinton et al. 2017; eBOSS Collaboration et al. 2020). Recently, it

Corresponding author: Yougang Wang
wangyg@bao.ac.cn

Corresponding author: Xin Zhang
zhangxin@mail.neu.edu.cn

Corresponding author: Xuelei Chen
xuelei@cosmology.bao.ac.cn

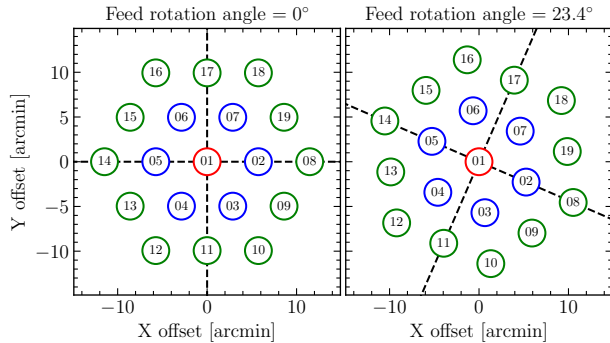


Figure 1. The position of the feed in the FAST L-band 19-feed array. The feed array without rotation is shown in the left panel and the feed array rotated by 23.4° is shown in the right panel. The circles represent the 3 arcmin beam size at frequency of 1420 MHz. The central, inner-circle, and outer-circle feeds are shown in red, blue, and green, respectively.

has been proposed another cosmological probe of the LSS by observing the neutral hydrogen (HI) in the galaxies via its 21 cm emission line of hyperfine spin-flip transition (e.g. Battye et al. 2004; McQuinn et al. 2006; Pritchard & Loeb 2012).

A number of HI galaxy surveys have been carried out, e.g. the 64 m Parkes telescope in Australia with the HI Parkes All-Sky Survey (HIPASS; Barnes et al. 2001; Meyer et al. 2004; Zwaan et al. 2004), the 76 m Lovell Telescope at Jodrell Bank with the HI Jodrell All-Sky Survey (HIJASS; Lang et al. 2003), the Arecibo Legacy Fast ALFA (ALFALFA) survey (Giovanelli et al. 2005, 2007; Saintonge 2007) and Jansky Very Large Array (JVLA) 10 deg² deep survey (Jarvis et al. 2014). However, limited by the sensitivity and the angular resolution of the radio telescopes, the redshift range of these surveys is much smaller than the current optical surveys. To resolve the HI emission line from individual distant galaxies at centimeter wavelength requires a large radio interferometer and it is time-consuming. Instead, a technique known as HI intensity mapping (HI IM), which is to measure the total HI intensity of many galaxies within large voxels (Chang et al. 2008; Loeb & Wyithe 2008; Mao et al. 2008; Pritchard & Loeb 2008; Wyithe & Loeb 2008; Wyithe et al. 2008; Peterson et al. 2009; Bagla et al. 2010; Seo et al. 2010; Lidz et al. 2011; Ansari et al. 2012; Battye et al. 2013), can be quickly carried out and extended to very large survey volume and is ideal for cosmological surveys (Xu et al. 2015; Zhang et al. 2021; Jin et al. 2021; Wu & Zhang 2022; Wu et al. 2022b,a; Zhang et al. 2023).

The HI IM technique was explored by measuring the cross-correlation function between an HI IM survey carried out with Green Bank Telescope (GBT) and an optical galaxy survey (Chang et al. 2010). Later, a few detections of the cross-correlation power spectrum between an HI IM survey and an

optical galaxy survey were reported with GBT and Parkes telescopes (Masui et al. 2013; Anderson et al. 2018; Wolz et al. 2017, 2022; CHIME Collaboration et al. 2022). There are several ongoing HI IM experiments focusing on the post-reionization epoch, such as the Tianlai project (Chen 2012; Li et al. 2020; Wu et al. 2021; Perdureau et al. 2022; Sun et al. 2022), the Canadian Hydrogen Intensity Mapping Experiment (CHIME, Bandura et al. 2014). A couple of HI IM experiments are under construction, such as the Baryonic Acoustic Oscillations from Integrated Neutral Gas Observations (BINGO, Battye et al. 2013) and the Hydrogen Intensity and Real-Time Analysis experiment (HIRAX, Newburgh et al. 2016). The HI IM technique is also proposed as the major cosmology project with the Square Kilometre Array (SKA)¹ (Santos et al. 2015; Square Kilometre Array Cosmology Science Working Group et al. 2020) and MeerKAT (Bull et al. 2015; Santos et al. 2017; Li et al. 2021; Wang et al. 2021; Paul et al. 2021; Chen et al. 2023). Recently, the MeerKAT HI IM survey reported the cross-correlation power spectrum detection with the optical galaxy survey (Cunnington et al. 2022). Meanwhile, using the MeerKAT interferometric observations, Paul et al. (2023) reports the HI IM auto power spectrum detection on Mpc scales. The HI IM auto power spectrum on large scales remains undetected (Switzer et al. 2013).

The Five-hundred-meter Aperture Spherical radio Telescope (FAST, Nan et al. 2011; Li & Pan 2016) was recently built and operating for observations (Jiang et al. 2020). FAST is located in Dawodang karst depression, a natural basin in Guizhou province, China (E 106°86, N 25°65). The FAST can reach all parts of the sky within 40° from the zenith, corresponding to ~ 25000 deg² sky area. With the 300 m effective aperture diameter, FAST becomes the most sensitive radio telescope in the world. In the meanwhile, the L-band 19-feed receiver, working at frequencies between 1.05 GHz and 1.45 GHz, increases the field of view, which is ideal for the large-area survey. Additionally, with ~ 3 arcmin angular resolution, the large area survey with FAST can potentially resolve the HI environment in a large number of galaxy clusters, groups, filaments, and voids.

Forecasts and simulations show that the large area HI IM survey with the FAST is ideal for cosmological studies (Li & Ma 2017; Hu et al. 2020). Before committing to a large survey, we proposed a pilot survey. With the pilot survey, we aim to find out the relevant characteristics of FAST receiver system. The systematic $1/f$ -type gain variation is studied in Hu et al. (2021). In this work, we address the time-ordered data (TOD) analysis pipeline for the HI IM with FAST drift-scan observation. This paper is organized as follows: We

¹ <https://www.skao.int>

Table 1. Observation mode. Column (1): The observation date. Column (2): The sample rate for recording the data. Column (3): The level of noise diode. Column (4): The rotated angle of the feed array.

Field center	Date	Frequency resolution [kHz]	Integration time [s]	Noise diode level	Rotation angle [°]
HIMGS 1100+2539	2019-05-27	0.5	1	high	0
HIMGS 1100+2554	2019-05-28	0.5	0.1	high	0
HIMGS 1100+2609	2019-05-29	7.6	0.1	low	0
HIMGS 1100+2554	2019-05-30	7.6	1	low	0
HIMGS 1100+2639	2019-05-31	7.6	1	low	23.4
HIMGS 1100+2639	2020-05-08	7.6	1	low	23.4
HIMGS 1100+2600	2021-03-02	7.6	1	low	23.4
HIMGS 1100+2632	2021-03-05	7.6	1	low	23.4
HIMGS 1100+2643	2021-03-06	7.6	1	low	23.4
HIMGS 1100+2654	2021-03-07	7.6	1	low	23.4
HIMGS 1100+2610	2021-03-09	7.6	1	low	23.4
HIMGS 1100+2621	2021-03-13	7.6	1	low	23.4
HIMGS 1100+2610	2021-03-14	7.6	1	low	23.4

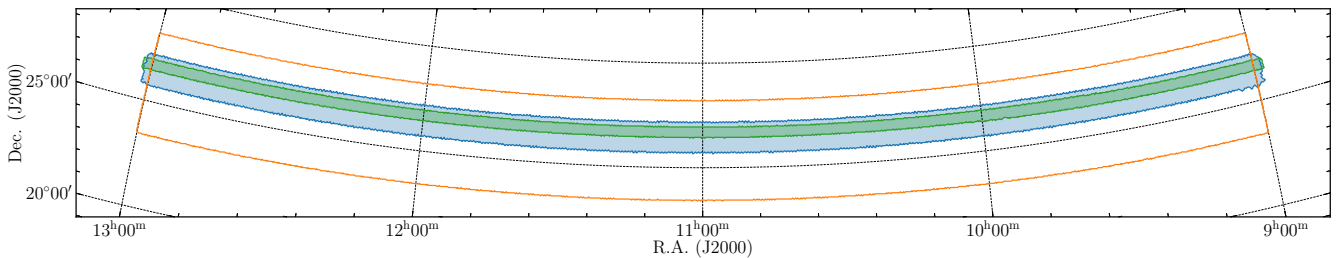


Figure 2. The footprint of the FAST H I IM Pilot Survey observation using Zenith equal area projection (ZEA). The filled blue region shows the sky area of the major data observed in 2021; The green stripe indicates the test observation carried out on May 31st, 2019 and May 8th, 2020; and the orange region shows the full target area for FAST H I IM Pilot Survey.

describe the data collected for H I IM pilot survey in Section 2 and the TOD analysis method in Section 3. The results and implications of the TOD analysis are discussed in Section 4. In Section 5 a summary of this work is presented.

2. OBSERVATIONAL DATA

The data analyzed in this work were collected in night sessions spanning in 2019, 2020 and 2021. During the observation of each night, the telescope was pointed at a fixed altitude angle. We chose an area close to the zenith, corresponding to Dec. $\sim 26^\circ$ at the telescope site. The resulting Dec. in the J2000 equatorial coordinate varies slightly (at a magnitude of ~ 3 arcmin) during the 4 hours drift-scan.

During the observations in 2019 and 2020, we investigated different configurations of the observation parameters, e.g the frequency resolution, sampling rate, feed array rotation angle and the level of the noise diode power, to test the impacts on the observation results. The finer resolution in frequency and time is beneficial for identifying narrow radio frequency in-

terference (RFI) and resolving the spectroscopic profile of H I galaxy. However, it produces a significant amount of data and takes a long time to process. Our testing results show that, with the exception of a few badly contaminated frequency ranges, RFI contamination can be properly detected utilizing the frequency resolution of 7.6 kHz. In the meanwhile, the spectral features of interest can be resolved using this frequency resolution. Data with finer frequency resolution and higher sampling rates are used for measuring the systematic $1/f$ noise at different temporal and spectroscopic scales. Our analysis (Hu et al. 2021) show that the systematic $1/f$ noise is negligible within a few hundred seconds time scale. Thus, we adopt 7.6 kHz frequency resolution and 1 s integration time for the survey observations.

We use the FAST L-band 19-feed receiver. The position of the feed in the 19-feed array is shown in Figure 1 The feed array is rotated by 23.4° to obtain the maximum span of Dec. coverage during the drift scans (Li et al. 2018). We also have a couple of observations without rotating the feed

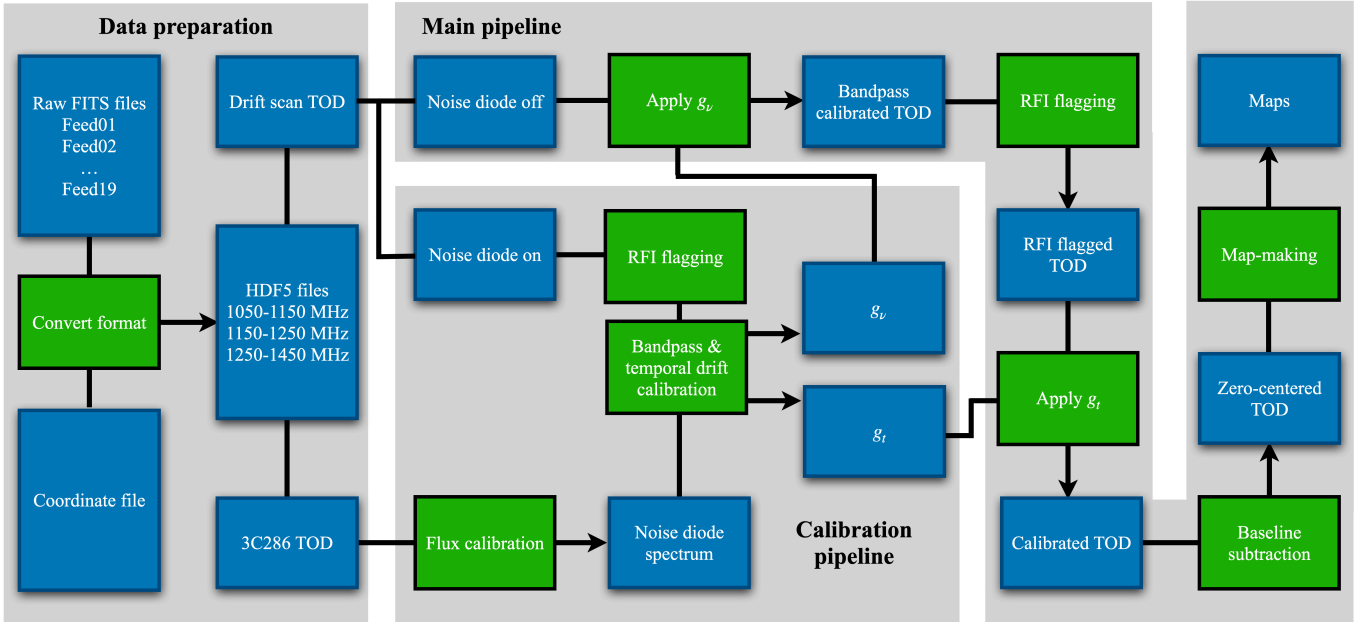


Figure 3. TOD analysis pipeline. The blue rectangular indicates the input/output data and the green rectangular indicates the operation.

array. During such drift-scan observations, the same sky stripe is repeatedly scanned by different feeds, which is ideal for systematic checking via cross-correlating the observation of different feeds.

A noise diode is built into the receiver system and its output can be injected as a real-time calibrator during the observation. In every 8 s, the noise diode was fired for 0.9 s, which is slightly shorter than the integration time to avoid power leakage to the nearby time stamps. In addition, the noise diode spectrum is calibrated by observing the celestial point source calibrator 3C286. The noise diode calibrator can be fired at either the high-power or the low-power level. With our test data, we found that the low-power level is sufficient for our calibration.

The observation of the 7 nights in 2021, that adopt the optimized observation parameter configuration, are the major survey data used in these analyses below. The pointing direction shifts by 10.835 arcmin per night in Dec. direction. With the 7 nights drift-scan observations, a range of $\sim 1^\circ$ across the Dec. direction is covered. With 4 hours drift scan, the observation covers the right ascension (R.A.) range from 9 hr to 13 hr, which overlaps with the Northern Galactic Cap (NGP) area of the Sloan Digital Sky Survey (SDSS; Reid et al. 2016). The detailed observation information is summarized in Table 1. The observation footprints of different data sets are shown in Figure 2.

The raw data of the 19 feeds are dumped into files individually using FITS² (Flexible Image Transport System) format. Each FITS file contains a chunk of TOD with all frequency channels. The telescope-pointing direction data are recorded separately. In order to simplify data analysis, we convert the initial data format by combining the 19-feeds data as an extra axis and splitting the full frequency band into three sub-bands, i.e. the low-frequency band 1050–1150 MHz, mid-frequency band 1150–1250 MHz and high-frequency band 1250–1450 MHz. The telescope pointing directions of the 19 feeds at each time stamp is calculated and written into the same data file.

The observation data include both the drift-scan data and the flux calibration data. The noise diode signal is used for real-time relative calibration of the gain, which is discussed in Section 3.1 and Section 3.2. The noise diode flux spectrum is calibrated by observing a standard source, as discussed in Section 3.3. The RFI flagging is applied to the calibrated data. The details of the RFI flagging are described in Section 3.5. The data are then zero-centered by removing the temporal baseline variation before being used for map-making. The TOD data analysis pipeline is illustrated in Figure 3, where the blue rectangular indicates the input/output data and the green rectangular indicates the operation.

3.1. Bandpass calibration

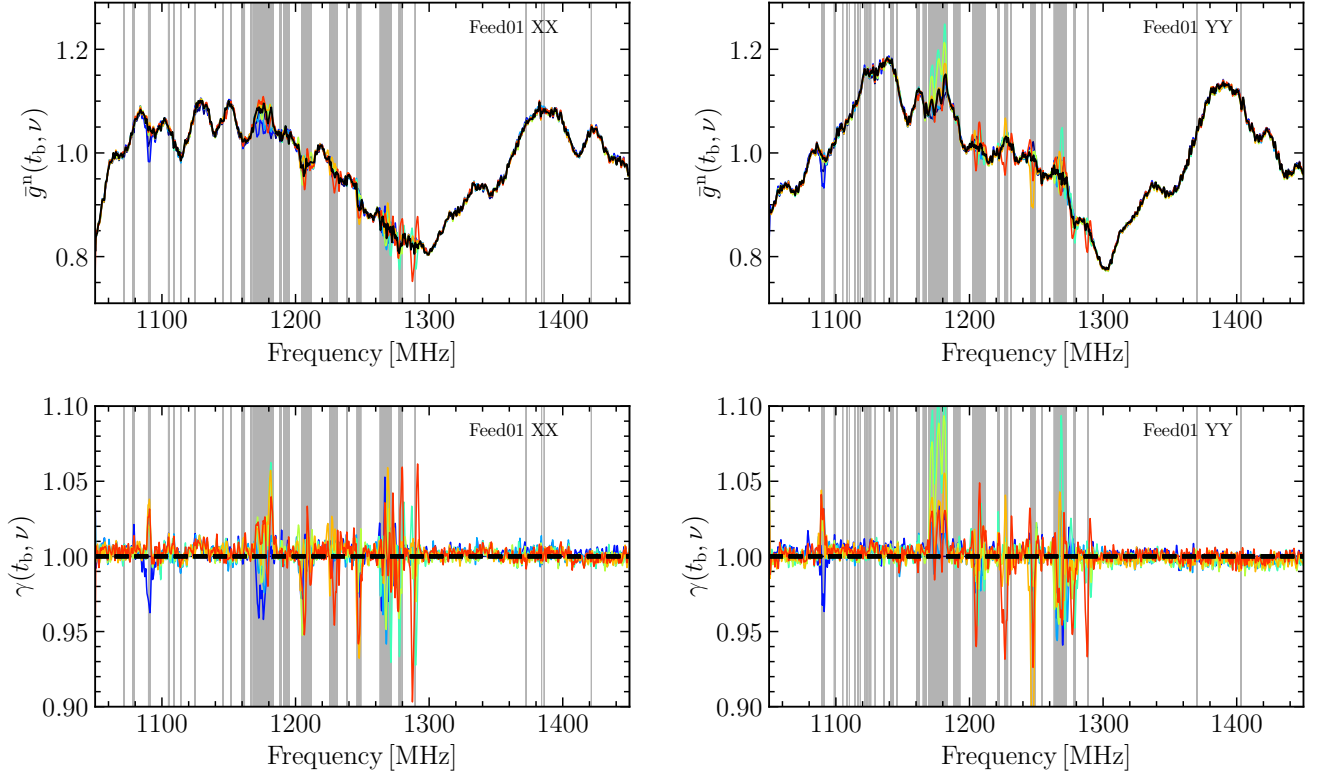


Figure 4. The smoothed bandpass of the XX (left) and YY (right) polarizations for the 20210302 data (i.e. those taken on March 2nd, 2021). The raw frequency resolution is 7.6 kHz, Top: The block averaged bandpass, each block is shown in a different color, and the black curve shows the averaged bandpass across all blocks. Bottom: the bandpass relative variation with respect to the first block. The gray areas mark the frequency channels with over 20% time stamps flagged.

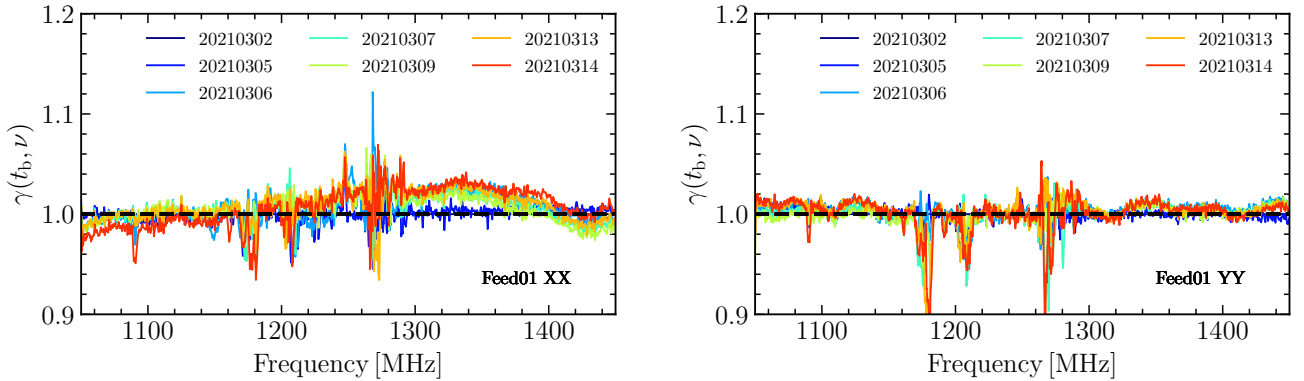


Figure 5. The bandpass relative variation between different nights with respect to the first night observation (20210302).

The observed data value, $V(t, \nu)$, is the system gain multiplied with the combination of the input signal and noise,

$$V(t, \nu) = g(t, \nu) (T(t, \nu) + n(t, \nu)), \quad (1)$$

where $T(t, \nu)$ is the antenna temperature corresponding to the total power collected by the telescope, $n(t, \nu)$ is the noise with $\langle n(t, \nu) \rangle_t = 0$, and $g(t, \nu)$ is the system gain. We assume that

the system gain can be decomposed into a time-dependent component and a frequency-dependent component:

$$g(t, \nu) = g_t(t)g_\nu(\nu), \quad (2)$$

where $g_\nu(\nu)$ is the bandpass gain factor and $g_t(t)$ is the temporal drift factor of the gain. In our analysis, $g_\nu(\nu)$ and $g_t(t)$ are calibrated using the noise diode, which is fired for 0.9 s in every 8 s as a relative flux calibrator. We assume that the noise diode temperature and spectrum are both stable during the ob-

servation. In every 8 s, we pick up the power value when the noise diode fired on, $V_{\text{NDon}}(t, \nu)$, subtract the average power value at the two nearby time stamps, $V_{\text{NDoff}}(t, \nu)$,

$$V_{\text{NDon}}(t, \nu) - V_{\text{NDoff}}(t, \nu) = g_t(t)g_\nu(\nu) (T_{\text{ND}}(\nu) + n(t, \nu)), \quad (3)$$

in which, we assume both g_t and the background emission are constant during the short time interval.

To check if the gain variation can be decomposed into factors of time variation and constant spectral shape as in Eq.(2), we break the full drift scan into a few of ~ 30 min time blocks (t_b) and evaluate the block-averaged bandpass gain,

$$\bar{g}(t_b, \nu) = \frac{\langle V_{\text{NDon}}(t, \nu) - V_{\text{NDoff}}(t, \nu) \rangle_{t_b}}{T_{\text{ND}}(\nu)}, \quad (4)$$

where $\langle \dots \rangle_{t_b}$ represent the averaging across the time block and $T_{\text{ND}}(\nu)$ is the noise diode spectrum.

The block-averaged bandpass is contaminated by the RFI. To remove the RFI contamination, we first smooth the data by applying a median filter across the frequency channels to obtain an estimation of the bandpass, then estimate the root mean square (rms) of the residual of the data after subtracting the smooth bandpass. The frequency channels with values greater than 3 times the rms are flagged as RFI contaminated. We iterate the flagging until there are no extra masked channels. Note that the RFI flagging processing applied to the bandpass determination procedure is much more strict than that applied to the survey data. Some of the flagged channels here may actually not be real RFIs. However, it does not hurt to take a more strict criterion in the bandpass determination. The RFI flagging is applied at each time stamp and the block-averaged bandpass is determined by taking the median value across the time block. A few of the frequency channels that are badly contaminated by RFI are fully flagged. The bandpass values at the fully flagged frequency channels are interpolated from the smoothed bandpass. Finally, in order to eliminate the noise, the bandpass is further smoothed with a 3rd-order Butterworth low-pass filter with a critical delay frequency of $\tau = 0.7 \mu\text{s}$, which corresponds to a window size of 200 frequency bins. The choice of the window function size is further discussed in Section 4.1.

The overall gain drift of the block-averaged bandpass, as well as the noise diode spectrum is removed by normalizing $\bar{g}(t_b, \nu)$ with its mean and produce the normalized bandpass,

$$\bar{g}^n(t_b, \nu) = \bar{g}(t_b, \nu) / \langle \bar{g}(t_b, \nu) \rangle_\nu, \quad (5)$$

where $\langle \dots \rangle_\nu$ represent the averaging across the frequencies. In order to visualize the bandpass shape evolution, we check the normalized bandpass ratio with respect to the first block,

$$\gamma(t_b, \nu) = \bar{g}^n(t_b, \nu) / \bar{g}^n(t_0, \nu), \quad (6)$$

where t_0 denotes the first time block.

An example of the results of Feed 01 for observation 20210302 (i.e. those taken on March 2nd, 2021) is shown in Figure 4, and different time blocks are represented by different colors. The black curve is the mean bandpass across all time blocks. The gray areas mark the frequency channels with over 20% time stamps flagged. As shown by this figure, the bandpass has significant variation over frequency and also varies with time, but its shape is nearly constant over a few hours, except for a small fraction of frequency channels, which are badly contaminated by RFI. The bottom panels show the bandpass ratio $\gamma(t_b, \nu)$, which has a variation less than 1% over 4 hr observation for most frequency channels.

Assuming the stable bandpass shape, Equation (3) is further averaged across the 4 hours of each night observation,

$$\langle V_{\text{NDon}}(t, \nu) - V_{\text{NDoff}}(t, \nu) \rangle_t = \bar{g}_t g_\nu(\nu) T_{\text{ND}}(\nu), \quad (7)$$

where $\bar{g}_t = \langle g_t(t) \rangle_t$. The bandpass relative variation between the seven nights observations in 2021 is shown in Figure 5. As an example, we show the two polarizations of the center feed in the left and right panels. The bandpass shape varies significantly between different days. Therefore, we emphasize that the bandpass shape needs to be determined for each night observation.

The bandpass-calibrated data is given by

$$V_1 \equiv \frac{V(t, \nu)}{\langle V_{\text{NDon}}(t, \nu) - V_{\text{NDoff}}(t, \nu) \rangle_t} = \frac{g_t(t)}{\bar{g}_t} \frac{T(t, \nu) + n(t, \nu)}{T_{\text{ND}}(\nu)}. \quad (8)$$

3.2. Temporal drift calibration

The temporal drift is calibrated with the noise diode as well. We average Equation (3) across frequencies,

$$\langle V_{\text{NDon}}(t, \nu) - V_{\text{NDoff}}(t, \nu) \rangle_\nu = \bar{g}_\nu g_t(t) (\langle T_{\text{ND}}(\nu) \rangle_\nu + n(t)), \quad (9)$$

where $\bar{g}_\nu = \langle g(\nu) \rangle_\nu$ and $n(t) = \langle n(t, \nu) \rangle_\nu$. If we further normalize with the time mean, the temporal drift is,

$$V_t = \frac{\langle V_{\text{NDon}}(t, \nu) - V_{\text{NDoff}}(t, \nu) \rangle_\nu}{\langle V_{\text{NDon}}(t, \nu) - V_{\text{NDoff}}(t, \nu) \rangle_{\nu, t}} = \frac{g_t(t)}{\bar{g}_t} + n'(t), \quad (10)$$

where we assume that both \bar{g}_ν and T_{ND} are constant over time and $n'(t) = (g_t(t) / \bar{g}_t T_{\text{ND}}) n(t)$. The first term of Equation (10), i.e. the normalized gain, represents the drifting of the actual gain, while the second term represents the variation caused by the measurement error in the calibration. V_t represents the measurements of the gain value at each firing of the noise diode. Written in discrete form, we denote the gain

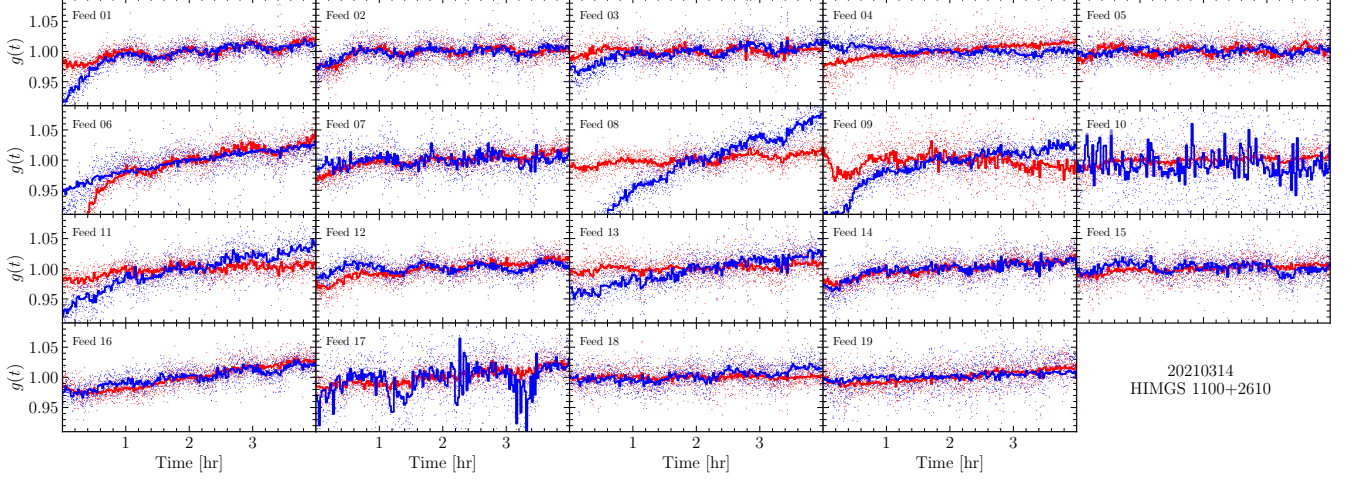


Figure 6. The gain temporal variations of 4 hours observation. Each sub-panel shows the gain of one feed, the two polarizations are shown in red and blue colors. The dot markers represent the measurements with the noise diode; and the thick curves are the reconstructed gain variation.

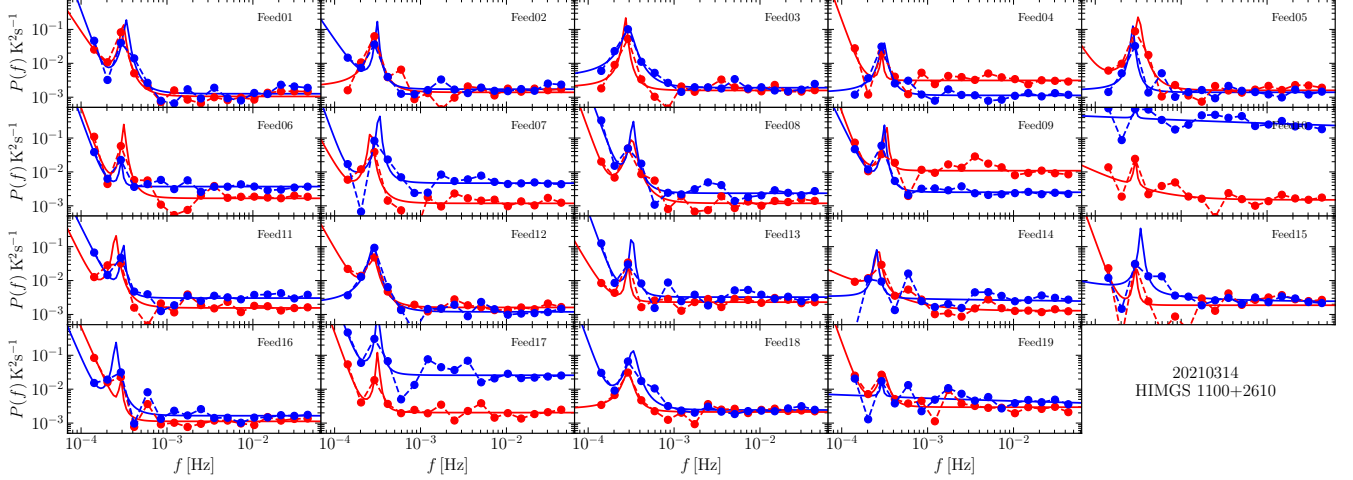


Figure 7. The temporal power spectra of the time-ordered data. Each sub-panel shows the gain of one feed, the two polarizations are shown in red and blue colors. The dashed lines with markers show the measured power spectra and the solid lines show the best-fit model of Equation (17).

measurements V_t as vector \mathbf{g}_m and Equation (10) is expressed as

$$\mathbf{g}_m = \mathbf{g}_t + \mathbf{n} \quad (11)$$

We split the full-time stream into α short time blocks, Δ_α . The gain is assumed to be constant within each short block and varying between different blocks. Using a set of the base function $\mathbf{F} = \{F_1(t), F_2(t), \dots, F_\alpha(t)\}$, where

$$F_\alpha(t) = \begin{cases} 1 & t \in \Delta_\alpha, \\ 0 & \text{otherwise,} \end{cases} \quad (12)$$

the drifting of the gain is expressed as $\mathbf{g}_t = \mathbf{F}\mathbf{g}$, where $\mathbf{g}^T = \{g_1, g_2, \dots, g_\alpha\}$ is the parameter sets that need to be determined. In our analysis, we use a short block length of

$\Delta_\alpha = 20$ s to avoid overfitting the temporal variation of the gain.

With the amplitude vector \mathbf{g} as the parameter, and the measured gain values \mathbf{g}_m , the likelihood is

$$P(\mathbf{g}_m) = P(\mathbf{g}_m|\mathbf{g})P(\mathbf{g}) \\ \propto \exp\left(-\frac{1}{2}\mathbf{n}^T\mathbf{N}^{-1}\mathbf{n}\right) \exp\left(-\frac{1}{2}\mathbf{g}^T\mathbf{C}_g^{-1}\mathbf{g}\right), \quad (13)$$

where \mathbf{N} is the measurement noise covariance matrix, and $\mathbf{C}_g = \langle\mathbf{g}\mathbf{g}^T\rangle$ is the covariance matrix of the gain amplitude vector. The temporal variation can be modeled as follows:

$$\mathbf{C}_g = \left(\mathbf{F}^T\mathbf{F}\right)^{-1} \mathbf{F}^T\mathbf{C}_N\mathbf{F} \left(\mathbf{F}^T\mathbf{F}\right)^{-1}, \quad (14)$$

where the covariance matrix \mathbf{C}_N is related to the noise power spectrum $P(f)$ as,

$$\mathbf{C}_N(\delta t) = \int P(f) e^{2\pi i f \delta t} df. \quad (15)$$

Note that, $P(f)$ represents only the power spectrum of the correlated noise ($1/f$ noise), the total noise power spectrum is the combination of the white and correlated noise power spectrum, i.e. $P_{\text{total}}(f) = \frac{\sigma^2}{\delta\nu} (1 + P(f))$, where σ is the systematic rms and $\delta\nu$ is the frequency resolution (Harper et al. 2018; Li et al. 2021).

The amplitude vector \mathbf{g} can be solved by the maximum likelihood method as

$$\hat{\mathbf{g}} = \left(\mathbf{F}^T \mathbf{N}^{-1} \mathbf{F} + \mathbf{C}_g^{-1} \right)^{-1} \mathbf{F}^T \mathbf{N}^{-1} \mathbf{g}_m, \quad (16)$$

which is equivalent to Wiener filtering.

The measurements of g_m for observation on 20210314, as an example, are shown in Figure 6 with the dot markers, the frequency range between 1150 MHz to 1250 MHz is ignored due to the serious RFI contamination. The averaging bandwidth of two separated sub-bands is ~ 300 MHz in total. The measurements of different feeds are shown in different panels and the two polarizations are shown in red and blue colors, respectively. The corresponding temporal power spectrum is shown with the dashed lines in Figure 7. There is a peak in the power spectrum at $f \sim 3 \times 10^{-4}$ Hz., corresponding to an oscillation in V_t with period ~ 1 hour.³ Except for this, the power spectrum has the $1/f$ -type shape, which has higher power at the lower end of the f -axis. The $1/f$ -type shape power spectrum is due to the overall drift of the V_t across time. The $1/f$ noise power spectrum is finally modeled as the combination of the $1/f$ -type power spectrum and a Lorenz profile,

$$\begin{aligned} P_{\text{total}}(f) &= \frac{\sigma^2}{\delta\nu} (1 + P(f)) \\ &= \frac{\sigma^2}{\delta\nu} \left(1 + \left(\frac{f}{f_k} \right)^\alpha + \frac{B}{1 + ((f - f_{\text{peak}})/w)^2} \right), \end{aligned} \quad (17)$$

where, α , f_k , B , f_{peak} , and w are the parameters that need to be fitted with the measured power spectrum. The solid lines in Figure 7 show the best-fit power spectrum.

With the best-fit noise power spectrum, we can estimate \mathbf{g} and the temporal gain variation can be reconstructed with

$$\mathbf{g}_t = \mathbf{F}\mathbf{g}. \quad (18)$$

³ The cause of the ~ 1 hour period oscillation is unknown. However, such oscillation is only observed in the 2021 data and disappeared in the later observations.

The reconstructed temporal gains for observation 20210314 are shown with thick curves in Figure 6. The temporal gain variation is finally calibrated via

$$V_2 = V_1/g_t. \quad (19)$$

3.3. Absolute flux calibration

The absolute flux calibration is done by multiplying the temporal gain calibrated data V_2 with the noise diode spectrum,

$$T = V_2 \times T_{\text{ND}}, \quad (20)$$

where T is referred below as the calibrated data, and T_{ND} as the temperature of the noise diode. The noise diode temperature is measured via a series of hot load measurements (Jiang et al. 2020) and it is assumed to be stable during the observations. During our observations, we performed several absolute flux calibrations using known celestial calibrators.

The absolute flux calibrations were made in drift scan mode. The 19 feeds were grouped into 5 east-west lines. With 5 different pointings, the calibrator drifted across each feed in the same east-west line. To minimize systematic differences compared to the target field observation, a calibrator with its Dec. close to the target field is required. We chose 3C286 as our flux calibrator and performed the calibration observation after the target observation of each day. The calibration pointing direction is shown in Figure 8.

The observation time is long enough to have the calibrator fully transits across the beam. The great-circle distance between the pointing direction and the calibrator, θ , is calculated with,

$$\cos(\theta) = \sin(\delta_p) \sin(\delta_{\text{cal}}) + \cos(\delta_p) \cos(\delta_{\text{cal}}) \cos(\alpha_p - \alpha_{\text{cal}}), \quad (21)$$

where (α_p, δ_p) and $(\alpha_{\text{cal}}, \delta_{\text{cal}})$ are the R.A. and Dec. of the pointing direction and the calibrator, respectively. We use the data within the time range with $\theta < 3$ arcmin as the source-on power $V_{\text{on}}(\theta)$, and average across the time range with $\theta > 12$ arcmin as source-off power V_{off} .

During the calibration, the noise diode is also fired in the same way as the target field observation. The data are firstly calibrated against the noise diode power, V_{ND} , to cancel the bandpass gain. The corresponding main beam brightness temperature of the calibrator is

$$T_{\text{cal}} B(\theta) = \frac{V_{\text{on}}(\theta) - V_{\text{off}}}{V_{\text{ND}}} T_{\text{ND}}, \quad (22)$$

where $B(\theta) = \exp\left[-\frac{\theta^2}{2\sigma^2}\right]$ is the normalized beam pattern with $\sigma = \theta_{\text{FWHM}}/(2\sqrt{2\ln 2})$. The antenna temperature is converted from the source flux density via

$$T_{\text{cal}} = \frac{\eta_M \lambda^2}{2k_B \Omega_{\text{MB}}} S, \quad (23)$$

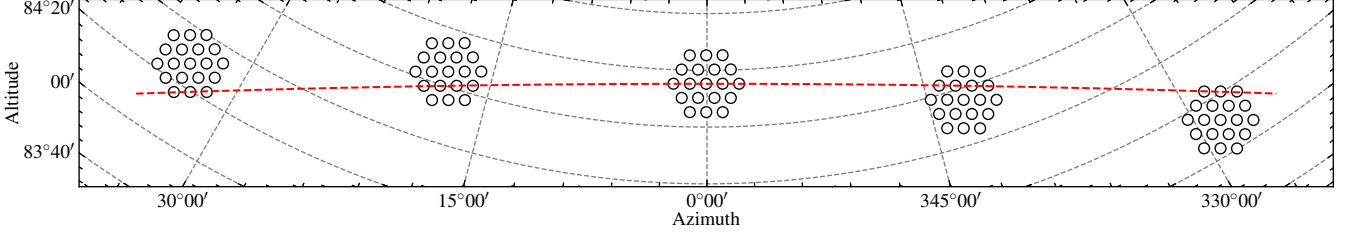


Figure 8. The footprint of the calibration observation. The red dashed line represents 3C286’s drift route as it crosses the meridian in the local alt-az coordinate at FAST site. The calibrator drifts through each line of feeds with five different pointing directions. The circles packed in hexagons illustrate the position of the 19 feeds in each pointing direction.

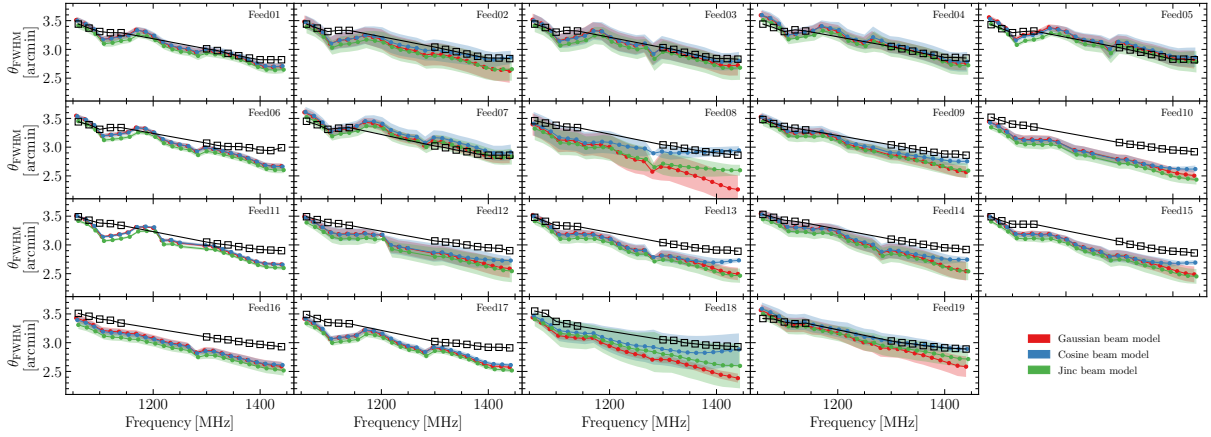


Figure 9. θ_{FWHM} measurements using 3C286 drift scan observation. The circle markers show the mean of the best-fit θ_{FWHM} across the measurements of different days and the filled region indicates the corresponding rms. The results of different beam models are shown in different colors. The black squares show the measurements from Jiang et al. (2020).

where k_B is the Boltzmann constant, λ is the wavelength, Ω_{MB} is the main beam solid angle and η_M is the main beam efficiency. Assuming a symmetric Gaussian beam with half power beam width θ_{FWHM} , the main beam solid angle is given by,

$$\Omega_{\text{MB}} = 2\pi \left(\frac{\theta_{\text{FWHM}}}{2\sqrt{2 \ln 2}} \right)^2 \approx 1.133\theta_{\text{FWHM}}^2, \quad (24)$$

The spectrum flux density of 3C286 can be modeled as Perley & Butler (2017),

$$\log \left(\frac{S}{\text{Jy}} \right) = 1.2481 - 0.4507x - 0.1798x^2 + 0.0357x^3, \quad (25)$$

in which, $x = \log \left(\frac{\nu}{\text{GHz}} \right)$. The noise diode spectrum is evaluated by minimizing the following residual function for each feed, frequency, and polarization,

$$\chi^2 = \sum_{\theta < 3 \text{ arcmin}} \left| \frac{\lambda^2 B(\theta) S}{2k_B \Omega_{\text{MB}}} - \frac{V_{\text{on}}(\theta) - V_{\text{off}}}{V_{\text{ND}}} \frac{T_{\text{ND}}}{\eta_M} \right|^2. \quad (26)$$

where T_{ND} is the parameter to be determined.

We can also leave the half power beam width, θ_{FWHM} , as another free parameter fit with the observation data. In order to model the sidelobes, we use the Jinc function beam model,

$$B_{\text{Jinc}} = 4 \left(\frac{J_1(\pi\theta/\theta_{\text{FWHM}})}{\pi\theta/\theta_{\text{FWHM}}} \right)^2, \quad (27)$$

where $J_1(x)$ is the Bessel Function of the First Kind; and the cosine beam model,

$$B_{\text{cos}} = \left(\frac{\cos(1.189\pi\theta/\theta_{\text{FWHM}})}{1 - 4(1.189\theta/\theta_{\text{FWHM}})^2} \right)^2, \quad (28)$$

which is known to have lower sidelobes compared to the Jinc function (Matshawule et al. 2020). We fit θ_{FWHM} at each frequency with initial frequency resolution of 7.6 kHz. In order to reduce the variance, the best-fit values are then averaged in each 16 MHz frequency bin. The best-fit θ_{FWHM} of the XX polarization from different beam models are shown in Figure 9 with different colors. The circle markers show the mean θ_{FWHM} across the measurements in different days and the filled region indicates the corresponding rms. The beam width reported in Jiang et al. (2020) is shown with the

black square markers. The best-fit θ_{FWHM} of Feed 01, which is in the center of the FAST 19-feed array shows consistent results across different days and beam models. Meanwhile, it is also consistent with θ_{FWHM} reported in Jiang et al. (2020). However, the best-fit results of the other feeds reveal significant scattering between various days, for example, Feed 02, or when using a different beam model, for example, Feed 08 and Feed 18. Some of the results, for example, Feed 10, show deviation from the results of Jiang et al. (2020).

A possible reason for this is that here we assumed a symmetric beam profile, but in reality, the beams are asymmetric. With a single transit observation, we can only measure the beam profile across one direction for both the XX and YY polarizations. As shown in Jiang et al. (2020), the full beam shape is significantly asymmetric and can be well fit using a 'skew Gaussian' profile, which takes into account the ellipticity. A complete analysis needs more observation and we will improve the measurements in further work. In the rest of the analysis, we interpolate the beam width using the results reported in Jiang et al. (2020).

Because the noise diode signal is injected into the receiver system between the feed and low-noise-amplifier (LNA) (Jiang et al. 2020), its sky-source-calibrated spectrum is slightly different from the noise diode spectrum model, which is measured using the hot-load. The difference is parameterized as,

$$\epsilon = \frac{T_{\text{ND}}^{\text{model}}}{T_{\text{ND}}}, \quad (29)$$

where $T_{\text{ND}}^{\text{model}}$ is the noise diode spectrum model and T_{ND} represents the noise diode spectrum determined using the celestial calibrator. In fact, ϵ degenerates with the main beam efficiency of FAST, η_{M} . Thus ϵ and η_{M} are combined as the total aperture efficiency $\eta = \eta_{\text{M}}\epsilon$ and determined using the celestial calibrator for each frequency, polarization, and feed.

It is known the aperture efficiency of FAST is weakly dependent on the Zenith Angle (ZA) with $\text{ZA} < 26^\circ 4'$; and decrease quickly with ZA beyond $26^\circ 4'$ (Jiang et al. 2020). Because our calibration observations were always carried out when 3C286 is near its transit time, the pointing directions of the same feed are relatively consistent between different days and the ZA are all within $26^\circ 4'$. Thus η is assumed to be relatively stable between days for our calibration observations. The measured η on different days are shown in Figure 10. Generally, the measured η varies between different feeds but keeps a similar shape between different days for the same feed. The measured η on each day is contaminated by RFI. In order to fill in the RFI gaps, we produce a template $\bar{\eta}$ for each feed by taking the median values of η across the measurements on different days and fitting with a 15th-order polynomial function. The η template is shown with the black solid line in Figure 10. To recover the variations of η between

different days, the η measurement on each day is fitted to the template via,

$$\eta = (p_0 + p_1\nu + p_2\nu^2 + p_3\nu^3)\bar{\eta}, \quad (30)$$

where $\{p_0, p_1, p_2, p_3\}$ are the parameters. The best-fit η for different measurements is shown in Figure 10 with solid curves in the same colors as the corresponding measurements. The sky absolute flux density is finally obtained as

$$T = V_2 \times T_{\text{ND}}^{\text{model}} / \eta. \quad (31)$$

3.4. Temporal baseline subtraction

We shall call the average of the calibrated data across the frequency band as the *baseline* of the data. The baselines for 6 days observation are shown in Figure 11 with different colors. The baselines are centered by subtracting the mean across the full observation time. The positive peaks in this data are due to bright continuum sources. Due to unknown reasons, some feeds occasionally perform badly during the observation, producing significantly larger fluctuations. Because different feeds point to different sky positions, we average the baselines across feeds to eliminate the flux variation from the sky. Such averaging across different feeds also reduces the baseline variance. Some of the data are contaminated by very strong RFI from satellites, which are fully flagged across the full frequency band. However, the data adjacent to these bad times are not flagged across the full frequency range. As the baseline is estimated by taking the median value across the frequency band, those partially flagged time stamps may have significantly lower median values than the rest, and result in negative spikes after subtracting the temporal mean.

In most cases, the baselines are steady, though the 20210306 data show some significant sharp variations, for which the reason is unknown. The shape of the baselines for different feeds is generally consistent as expected, even for the 20210306 observation. This might indicate the baseline variation is due to a systematic background noise level variation during the observation time. We take the median across the 19 baselines to get rid of the spikes and further smoothed across along the time with a median value filter. The smoothed mean baseline is shown with the thick black curve. The smoothed baseline is fit to the calibrated TOD at each frequency,

$$\mathbf{A} = \left(\mathbf{b}^T \mathbf{b} \right)^{-1} \mathbf{b}^T \mathbf{T}, \quad (32)$$

where \mathbf{b} represents the $n_t \times 1$ vector of baseline template, \mathbf{T} represents the $n_t \times n_\nu$ matrix of TOD and \mathbf{A} is the $1 \times n_\nu$ vector of the fitting parameter. The baseline is subtracted via

$$\mathbf{T}_\nu^c = \mathbf{T}_\nu - \mathbf{b}\mathbf{A}, \quad (33)$$

where T^c represent the baseline centred TOD.

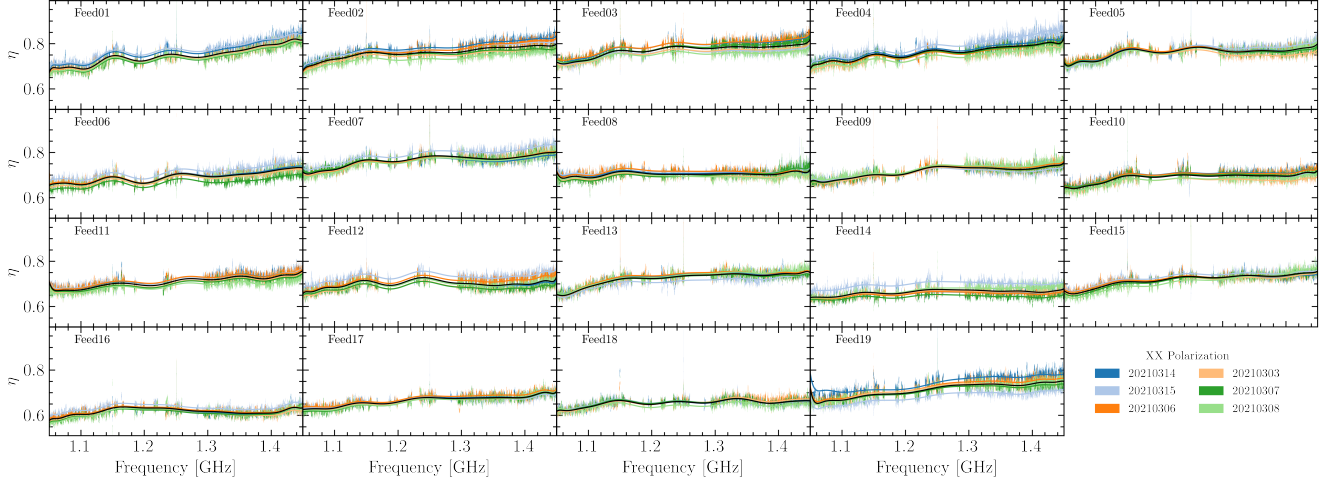


Figure 10. The best-fit η for different measurements;

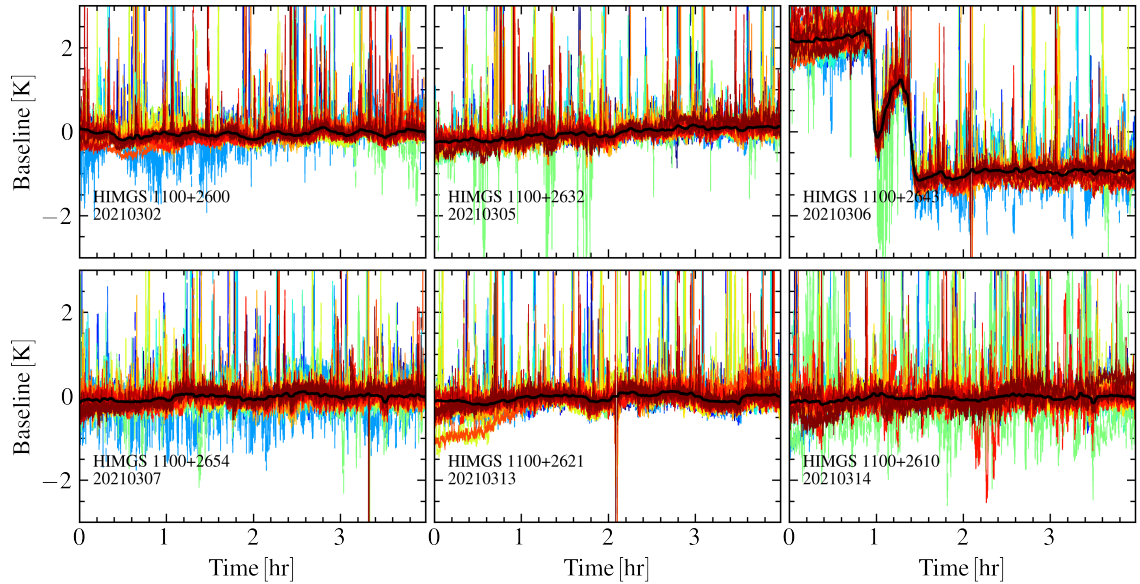


Figure 11. The temporal variation of baselines for the 6 days of observation. The different color shows different feeds. The temporal baselines for each feed are centered by subtracting the mean across the full observation, individually. The positive peaks are due to the bright continuum sources, and the few negative spikes are bad data due to the strong RFI contamination.

3.5. RFI flagging

In Figure 12, the black curve shows the spectrum from one feed averaged over ~ 30 min. There is strong RFI contamination in the frequency band between 1150 MHz to 1300 MHz, which are produced by the Global Navigation Satellite Systems (GNSS), including the GPS, Galileo, Glonass, and BeiDou (Teunissen & Montenbruck 2017). The frequency channels allocated for GNSS are marked in different colors. The contamination of such GNSS bands can leak into the neighboring channels due to the extended GNSS signal spectrum profile. We first remove the channels badly contaminated by GNSS, including those allocated frequency channels, as well

as the neighboring channels within $1 \sim 20$ MHz. The pre-removed frequency channels are shown with the gray area in Figure 12.

We then apply the SumThreshold and SIR (Scale-Invariant Rank) RFI flagging program (Offringa et al. 2010, 2012; Zuo et al. 2021) to the bandpass calibrated data. The SumThreshold algorithm searches for consecutive points of different numbers (increase from 1 to 2^n) in TOD as the potential RFI contaminated points which have value above certain preset thresholds, i.e. $\chi_n = \chi_1 / 1.5^{\log_2 n}$, where $\chi_1 = 10$ is the initial threshold and n is the number of data sample considered. The thresholds are varying according to the number

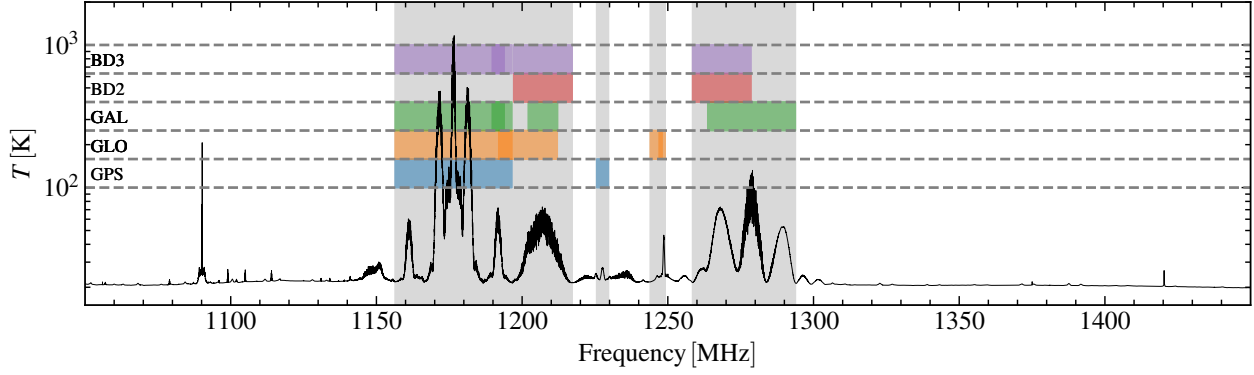


Figure 12. The spectrum from a feed averaged over ~ 30 min. The channels contaminated by RFI from GNSS are marked by the gray region. The allocated frequency channels used for the GPS, Galileo (GAL), Glonass (GLO), and Beidou (BD2/BD3) are marked in different colors (Teunissen & Montenbruck 2017).

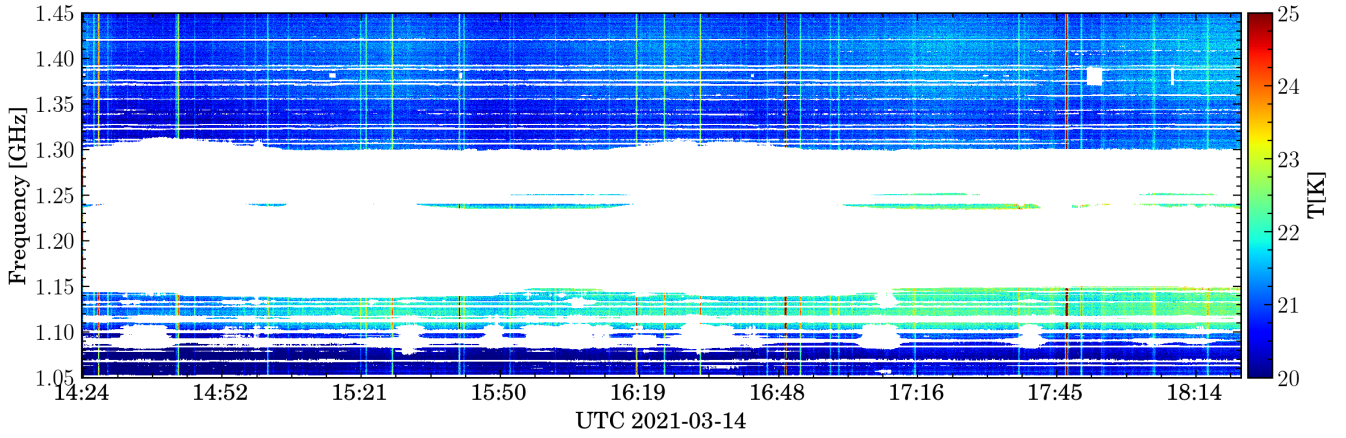


Figure 13. Waterfall plot of ~ 4 hr TOD observed with Feed01 XX polarization. The blank region is the RFI-flagged data.

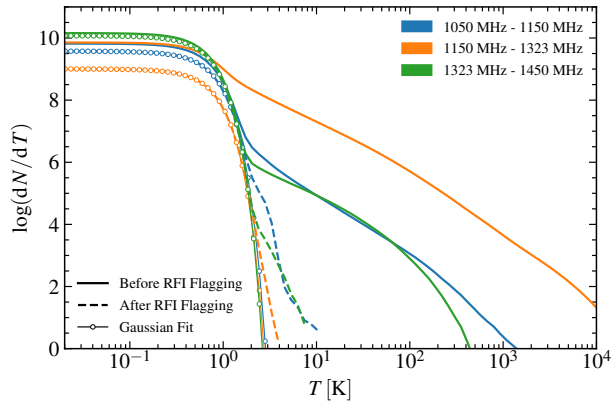


Figure 14. Histogram statistic of the temperature difference before and after the RFI flagging.

of data samples considered. In order to find the extra weak contamination near the flagged high values, the SIR RFI flagging is then applied. The SIR RFI flagging method uses the one-dimensional mathematical morphology technique to find

the neighbored intervals in the time or frequency domain that are likely to be affected by RFI.

Compared to other radio telescopes, the FAST is much more sensitive, with many genuine celestial radio sources, and even the HI emissions from nearby galaxies could be detected with a high signal-to-noise ratio (SNR) in the raw data, therefore, care must be taken to avoid removing them by mistake. We stack the same time outputs of the different feeds, which would lower the celestial source signal as the different feeds are pointed at slightly different sky directions at any given time while enhancing the RFIs which enter through the beam side lobe and are simultaneous on all feeds. Also, the SumThreshold algorithm is only applied along the frequency axis.

As an example, the RFI flagged 20210314 data for Feed01 XX polarization is shown in a waterfall plot Figure 13. The blank regions are flagged data. Most frequency bands between 1150 MHz and 1323 MHz are flagged as they are badly contaminated by the GNSS. Another severely RFI contaminate part is around 1090 MHz, which is the band allocated to

aircraft Automatic Dependent Surveillance-Broadcast (ADS-B) data communication, where the RFI occurs frequently during the 4-hour observation. The frequency range beyond 1323 MHz is relatively free of RFI.

To check the RFI residual after flagging, we show a histogram of the data. The contribution of natural continuum emission can be removed by taking the difference between the two neighboring frequency channels. The histograms are produced using data in three different frequency ranges, i.e. 1050 – 1150 MHz, 1150 – 1323 MHz and 1323 – 1450 MHz, and the results are shown in Figure 14. The results of the data before RFI flagging are shown with solid lines and those after RFI flagging is shown with dashed lines. Before RFI flagging, the data shows a combined profile of a Gaussian distribution and a high-temperature tail, which indicates a significant RFI contamination. After the RFI flagging, the high-temperature tails are greatly reduced in all three frequency bands. The histogram statistic also shows that, with the `SumThreshold` flagging, there are 34.7%, 79.2% and 12.2% data flagged in the three frequency bands, respectively; and with the additional SIR flagging, another 6.5%, 8.5% and 2.0% data are flagged. For the data on other days, the ratios are more or less similar.

The frequency channels within 1150-1323 MHz are badly contaminated by the strong RFI contamination. Especially, the channels at the lower-end of the frequency band, 1250-1450 MHz contain some GNSS signal bands. We adjust the valid frequency range of the high-frequency band to 1323-1450 MHz.

3.6. Maps

The calibrated data are zero-centered by subtracting the baseline and the XX and YY polarization are combined into Stokes I. The TOD is then projected to the map domain via the standard map-making procedure (Tegmark 1997). In order to save the computation time for map-making, we re-binned the data to 28 kHz frequency resolution. The maps are made for each frequency without considering the correlation between different frequency channels.

We use the variance across time of the ~ 30 min data block for each feed and polarization as the noise variance. The noise is assumed to be uncorrelated between different time blocks, and its covariance matrix is assumed to be diagonal, i.e. $\mathbf{N} = \text{diag}\{\sigma^2(t)\}$. The map is obtained by

$$\hat{\mathbf{m}} = (\mathbf{P}^T \mathbf{N}^{-1} \mathbf{P})^{-1} \mathbf{P}^T \mathbf{N}^{-1} \mathbf{T}, \quad (34)$$

in which, \mathbf{P} is the pointing matrix, which relates the time to the map coordinate. We use the HEALPix scheme for the sky with NSIDE = 2048, corresponding to a pixel size of 1.72 arcmin (pixel area of 2.95 arcmin²).

Figure 15 shows the frequency-averaged maps. The maps made with the data of two RFI-free frequency bands are shown

in the top and bottom panels, respectively. As the surveyed sky is a long strip, we divide the full region into several pieces in the R.A. direction, each is about 1 hr (i.e. 15°) in R.A. We can see many point sources on the map clearly, and the point sources in the 1050-1150 MHz band has good correspondence with the point sources in the 1323-1450 MHz band, which is what we would expect for the radio continuum sources such as quasars and radio galaxies.

In order to improve the flux measurements of point sources, we applied an alternative map-making procedure similar to Haynes et al. (2018)

$$\hat{m}_p = [(\mathbf{PK})^T \mathbf{T}]_p / [(\mathbf{PK})^T \mathbf{I}]_p, \quad (35)$$

where p indicate the p -th pixels of the map, $\mathbf{I} = \{1, 1, \dots, 1\}^T$ is a column vector with all elements equal to 1 and \mathbf{K} represents a kernel function that paints the antenna temperature to the nearby pixels. We use a Gaussian kernel function

$$K_{pq} = \exp \left[-\frac{1}{2} \left(\frac{r_{pq}}{\sigma_K} \right)^2 \right], \quad (36)$$

where K_{pq} the element of the \mathbf{K} matrix, r_{pq} is the great circle distance between the p -th and q -th pixels of the map and σ_K indicates the kernel size. We set $\sigma_K = 1.5$ arcmin and use HEALPix scheme with NSIDE = 4096, corresponding to a pixel size of 0.86 arcmin. To make the map-making process easier, the TOD from 1375 MHz to 1425 MHz are averaged into a single frequency channel before the map-making. Such a map is used for flux comparison with the continuum sources. We extract the flux of point sources and compare them with the NVSS continuum measurements. Finally, 81 isolated point sources with flux over 14 mJy are identified within the surveyed region. The flux measurements are presented in Table 3 and the detailed discussion can be found in Section 4.4.2.

As the observed data is already the convolution of the sky signal and the telescope beam pattern, using the kernel function Equation (36) to create the map is equivalent to an additional convolution. If we assume a Gaussian beam model with a beam width of θ_{FWHM} , the final map is then smoothed with a Gaussian function with a kernel size of $\sigma_{K'} = \sigma_K + \theta_{\text{FWHM}} / (2\sqrt{2 \ln 2})$.

4. DISCUSSION

4.1. Bandpass ripple

The bandpass calibration changes the shape of the spectrum significantly. To understand the ripple structure in the bandpass, we estimate the delay spectrum $|\tilde{V}(\tau)|^2 = \langle \delta\tilde{V}(\tau) \delta\tilde{V}^*(\tau) \rangle$, where

$$\delta\tilde{V}(\tau) = \int dv \delta V(v) e^{-2\pi i v \tau}$$

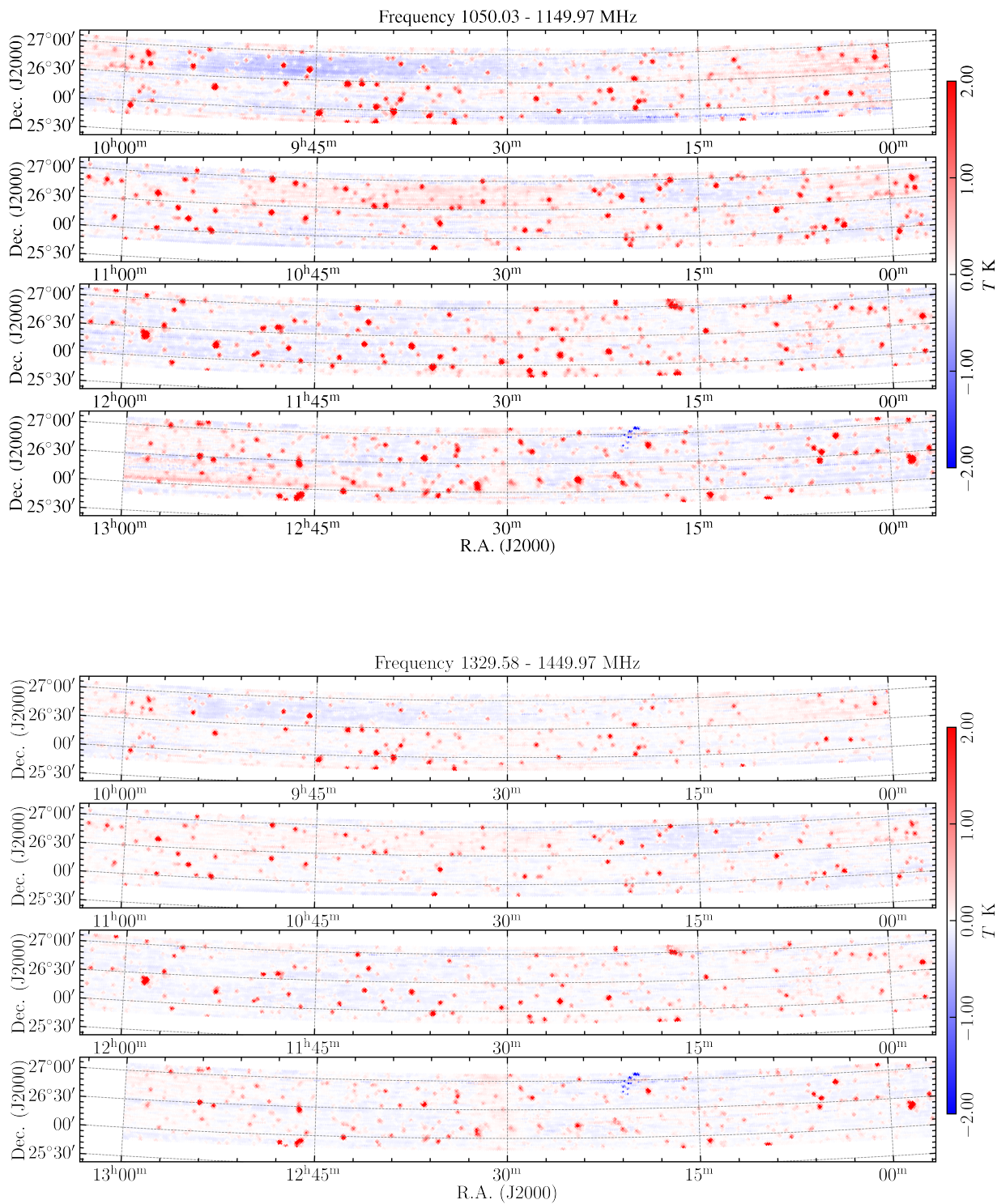


Figure 15. Total intensity map of the surveyed regions. The top and bottom panels show the integrated intensity between 1050-1150 MHz and 1323-1450 MHz respectively.

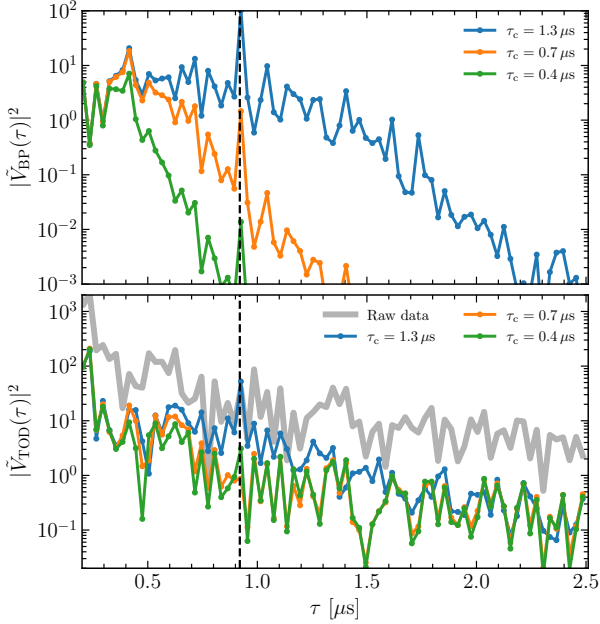


Figure 16. Top panel: the delay spectrum of the bandpass. The delay spectra of the bandpass smoothed with different window function sizes are shown in different colors. Bottom panel: the delay spectrum of the TOD. The gray curve shows the delay spectrum of the TOD before bandpass calibration, while the rest curves show the results of bandpass-calibrated data using bandpass measurement smoothed with different window function sizes. All the delay spectra are estimated using the XX polarization of the central beam data of 20210302. The dashed vertical line marks the delay of $\tau \sim 0.92 \mu\text{s}$, associated with the standing wave between the FAST feed and reflector.

is the Fourier transform of the data across the frequency. We make the analysis with the data contrast, i.e. $\delta V(\nu) = \frac{V(\nu)}{\bar{V}} - 1$, where $V(\nu) = \langle V(t, \nu) \rangle_t$ is the data value at frequency ν averaged across observation time, and $\bar{V} = \langle V(\nu) \rangle_\nu$ is the mean $V(\nu)$ averaged across the frequency band. The delay spectrum is taken for the data before the bandpass calibration, after bandpass calibration, and also for the measured bandpass itself. The bandpass ripple structure would show up as a peak in the delay spectrum at a particular delay value.

In Figure 16 we plot the delay spectra of the bandpass (top panel) and the data (bottom panel) of the XX polarization of the center feed during the 20210302 observation. The spectra for other feeds and polarizations are similar. For the bandpass (top panel), as mentioned in Section 3.1, we show the results of smoothing with the 3rd-order Butterworth low-pass filter of three different sizes (defined as the 3 dB compression point) $\tau_c = 1.3 \mu\text{s}$, $0.7 \mu\text{s}$ and $0.4 \mu\text{s}$, respectively. As expected, the delay spectra are strongly suppressed at the small scale by the smaller-sized filters. For the delay spectra, we show the raw data (i.e. TOD before calibration) and the calibrated data using the bandpass smoothed with the three different filter sizes.

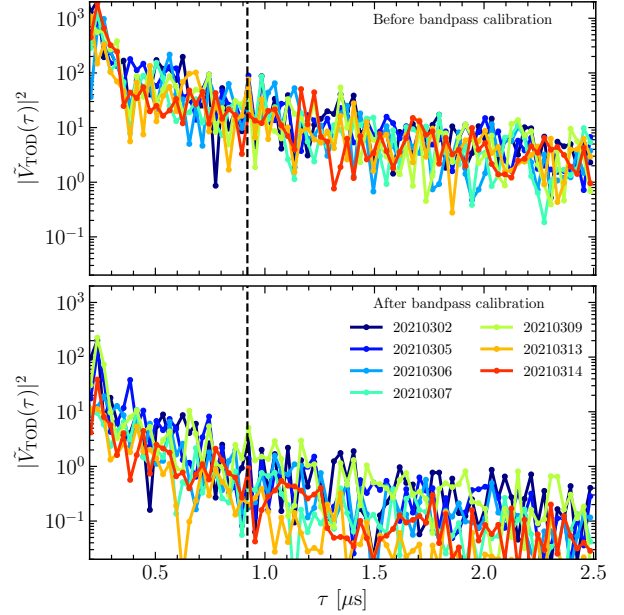


Figure 17. The TOD delay spectrum of different days. The top panel shows the delay spectra of the TOD before bandpass calibration, while the bottom panel shows the results after bandpass calibration. All the delay spectra are estimated using the XX polarization of the central beam data. The dashed vertical line marks the delay of $\tau \sim 0.92 \mu\text{s}$, associated with the standing wave between the FAST feed and reflector.

In the bandpass delay spectrum, we can see an obvious peak which is marked by a dashed vertical line in the figure. This peak is associated with a standing wave between the FAST feed and reflector, with a delay of $\tau \sim 0.92 \mu\text{s}$, corresponding to a standing wave with a ripple wavelength of 1.087 MHz in the spectrum. However, we do not see a significant standing-wave peak in the raw TOD, the standing-wave signature is more prominent in the bandpass measurements than in the sky observation, probably because this standing wave is induced by the noise diode itself. If the data is calibrated with such a bandpass, it would induce the ripple structure which is not present in the raw data itself. This can be avoided by employing the bandpass smoothed with small-sized filters, e.g. those with $\tau_c = 0.7 \mu\text{s}$ and $\tau_c = 0.4 \mu\text{s}$ filters, as shown in the bottom panel of Figure 16. Note the smoothing filter is applied to the bandpass, not the sky spectrum.

The delay spectra of the TOD before bandpass calibration for all seven nights are shown in the top panel of Figure 17. Two out of the seven nights' data show weak standing-wave peaks. The standing-wave signature is generally consistent across different polarization and beams within the same night's observation. We use the low-pass filter with the size of $\tau_c = 0.7 \mu\text{s}$ to suppress both the noise and standing-wave signature during the bandpass determination. The delay spectra

of the bandpass calibrated data are shown in the bottom panel of Figure 17, the standing-wave peak is negligible.

4.2. Measurement uncertainty

The system temperature T_{sys} , is related to the measurement noise level via the radiometer equation,

$$\sigma = \frac{T_{\text{sys}}}{\sqrt{N_{\text{pol}}N_{\text{feed}}\Delta t\Delta\nu}}, \quad (37)$$

where σ is the rms of the measurements representing the noise level, $N_{\text{pol}} = 2$ is the number of polarization, $\Delta t = 1$ s is the integration time, $\Delta\nu = 28$ kHz is the frequency resolution and N_{feed} is the number of the feed. We estimate the measurement noise level for each of the feeds individually and adopt $N_{\text{feed}} = 1$ in the following analysis.

To calculate the rms, we subtract the continuum emission of the point sources. We revise the rms estimation method introduced in Wang et al. (2021), that uses the difference between four adjacent frequency channels,

$$\Delta T(\tilde{\nu}) = \frac{1}{2}(T(\nu_1) + T(\nu_3)) - \frac{1}{2}(T(\nu_2) + T(\nu_4)), \quad (38)$$

where $\nu_1 < \nu_2 < \nu_3 < \nu_4$ are the four adjacent frequency channels and $\tilde{\nu} = (\nu_1 + \nu_2 + \nu_3 + \nu_4)/4$ is the reduced frequency of the residual data. This can remove most of the continuum emission from the sky that is linear across the frequencies. The rms of the residual data is related to the original data rms via,

$$\sigma(\tilde{\nu}) = \sqrt{\frac{1}{4}(\sigma^2(\nu_1) + \sigma^2(\nu_3)) + \frac{1}{4}(\sigma^2(\nu_2) + \sigma^2(\nu_4))}. \quad (39)$$

We calculate the noise level using the calibrated data. Each day's data is divided into seven blocks, each ~ 30 -minute; and the two polarizations are combined into the total intensity, i.e. $T = (T_{\text{XX}} + T_{\text{YY}})/2$. Figure 18 shows the histogram statistics of the residual data value. For each time block, the histogram statistic includes all the 19 beams' data and the result is shown with the gray curve. The histogram for all time blocks combined is shown with the green curve. All the histograms are normalized with the total number of data samples. The results of the low-frequency band, i.e. 1050-1150 MHz, are shown in the left panel, and the high-frequency band, i.e. 1323-1450 MHz, are shown in the right panel, respectively.

We fit the histogram with a Gaussian function,

$$N(T) = A \exp\left[-\frac{1}{2}\frac{(T - \mu_0)^2}{\sigma^2}\right]. \quad (40)$$

The best-fit function of the all-time-block combined histogram is shown with the dashed red curve in Figure 18 and

the best-fit σ and μ_0 are also shown in the legend. Both of the two frequency bands' data fit the Gaussian function well, which indicates that the residual data are dominated by white noise. The best-fit noise levels of the data are 116.39 mK and 99.47 mK for the low-frequency band and high-frequency band, respectively.

The system temperature includes several different components and can be expressed as,

$$T_{\text{sys}} = T_{\text{rec}} + T_{\text{sky}} + T_{\text{CMB}}, \quad (41)$$

where T_{rec} is the receiver temperature; T_{sky} is the sky temperature; and $T_{\text{CMB}} = 2.725$ K is the mean brightness temperature of the cosmic microwave background (CMB). We ignore the temperature from ground-spill when the telescope is pointing close to the Zenith. The major component of the T_{sky} is the diffuse emission of the Galactic synchrotron. According to the measurements in the work of Jiang et al. (2020), the system temperature close to the Zenith is about 20 K. Using Equation (37) and substituting $N_{\text{pol}} = 2$, $N_{\text{feed}} = 1$, $\Delta t = 1$ s and $\Delta\nu = 28$ kHz, we should have $\sigma = 84.5$ mK. The slightly higher noise level could be caused by residual continuum emissions.

The noise level also fluctuates between different feeds. As shown in Figure 20, the noise level of the lower and higher frequency bands are shown in red and blue markers. The feeds are split into three categories, i.e. the feeds in the central (Feed 01), the inner circle (Feed 02 - Feed 07) and the outer circle (Feed 08 - Feed 19) of the feed array. The horizontal lines indicate the mean noise level of each feed category. Although the noise levels of different feeds are varying, there is a trend that the feeds in the outer circle of the feed array have higher noise, i.e. about 10% increases in the noise level with respect to the central feed.

Such system temperature estimation can also be applied in the map domain. We estimate the pixel noise level of the map at each reduced frequency, $\tilde{\nu}$. The histogram of each reduced frequency is shown with the gray curve in Figure 19. The green curve shows the total histogram using all frequencies. The results of the low/high-frequency band are shown in the left/right panels. The dashed red curve shows the best-fit Gaussian function. Only histograms with amplitudes greater than half of their maximum are used in the Gaussian function fitting. The best-fit σ of the Gaussian function indicates the pixel noise level.

Clearly, the total histogram profile departs from the Gaussian function at $|T| \gtrsim 0.05$ K. The pixel noise level for the low-frequency and high-frequency bands are 36.0 mK and 25.9 mK, respectively. Because the fit only uses the histograms with amplitudes greater than half of their maximum, the pixel noise level does not take into account the effect of the large residual values. Nevertheless, the pixel noise level is higher than the forecast. Due to the different RFI flagging

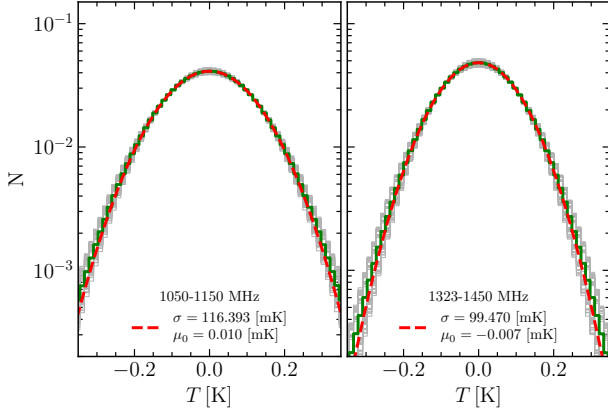


Figure 18. The histogram of the residual TOD. The solid green curve represents the combined data histogram and the dashed red line represents the best-fit Gaussian distribution. The gray thin curves represent the histograms of different data blocks. Each curve is normalized by its total number of data points.

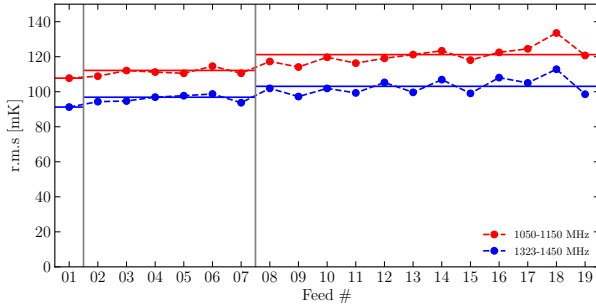


Figure 20. The noise level of each feed. The results for lower and higher frequency bands are shown in red and blue markers. The feeds are split into three categories, i.e. the feeds in the central (Feed 01), the inner circle (Feed 02 - Feed 07), and the outer circle (Feed 08 - Feed 19) of the feed array. The horizontal lines indicate the mean noise level of each feed category.

fractions, the mean integration times for the low-frequency and the high-frequency band are 10.0 s and 16.7 s, respectively. Thus, assuming $T_{\text{sys}} = 20$ K, the pixel noise levels for such two frequency bands are 26.8 mK and 20.7 mK, respectively. A couple of reasons could potentially increase the noise. For example, the weak RFI contamination, which is below the noise level of the original TOD, becomes dominant when the pixel noise level is lowered by integrating data via the map-making process; the residual sky contamination that is not removed with Equation (38); or the weakly correlated noise in the original TOD.

4.3. Spectra of sources

We also inspect the bandpass shape by comparing the spectra of bright sources to the flux measurements in the literature. We chose the bright sources that are closely scanned by at least one beam, i.e. the minimal angular distance between the source and the beam center is less than 0.5 arcmin. In

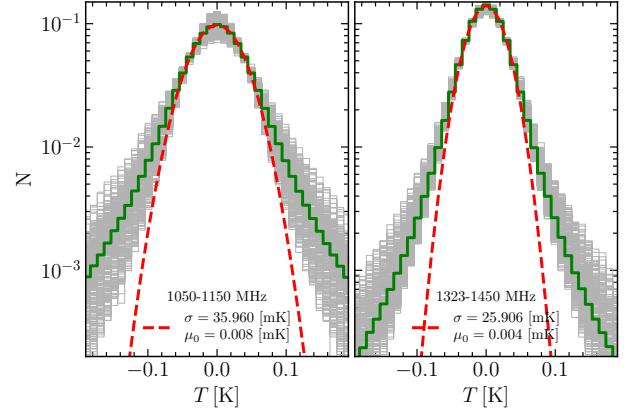


Figure 19. Same as Figure 18 but for the residual maps. The gray thin curves represent the histograms of different frequencies.

the meanwhile, the source should have flux measurements at multiple frequency bands. In this analysis, we use 10 radio sources with flux measurements at 74 MHz (Cohen et al. 2007), 151 MHz (Waldram et al. 1996), 365 MHz (Douglas et al. 1996), 408 MHz (Colla et al. 1972), 1.4 GHz (Condon et al. 1998), and 4.85 GHz (Becker et al. 1991). The flux of such 10 sources are listed in Table 2. The source spectrum is modeled by fitting a 3rd-order polynomial function to the flux measurements.

The source spectra are extracted from the calibrated data by taking the spectra at the time stamp when the source center is mostly close to the pointing direction. The data within the frequency band 1150–1250 MHz is ignored due to serious RFI contamination. The spectrum of each source is then averaged in every 10 MHz frequency bin. The measured spectra of the 10 sources are shown in Figure 21. The error bar indicates the rms of the flux measurements within each 10 MHz frequency bin. The polynomial-fitted source spectrum model is shown with the black dashed line and the gray area indicates the model uncertainty, i.e. the upper/lower bound is estimated by fitting the 3rd-order polynomial function to the upper/lower limit of 68% flux measurement confidence interval. The gap between 1150 MHz and 1300 MHz is due to RFI contamination.

Generally, our measurements produce a smooth power-law shape spectrum, which indicates that the bandpass calibration efficiently corrects the bandpass shape. The spectrum shape slightly fluctuated at frequencies close to the RFI contamination, especially for the relatively faint sources. The flux is generally consistent with the spectrum model fitted using the flux measurements at a few frequency bands in the literature. The deviation between our measurement and the spectrum model, e.g. source B2 1039+27, might be because

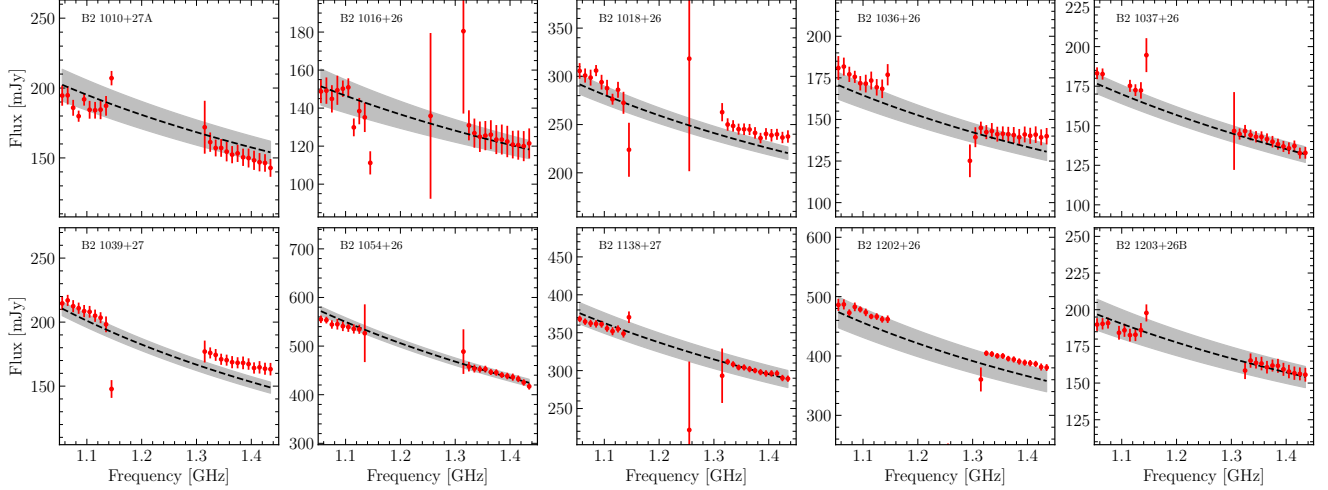


Figure 21. The spectra of bright sources in the field. The red markers show the measured source spectrum. The flux is averaged within each 10 MHz frequency bin and the error bar indicates the flux rms in each frequency bin. The gap between 1150 MHz and 1300 MHz is due to RFI contamination. The dashed line indicates the source spectrum model fit using flux measurements in the literature and the gray area indicates the spectrum model uncertainty.

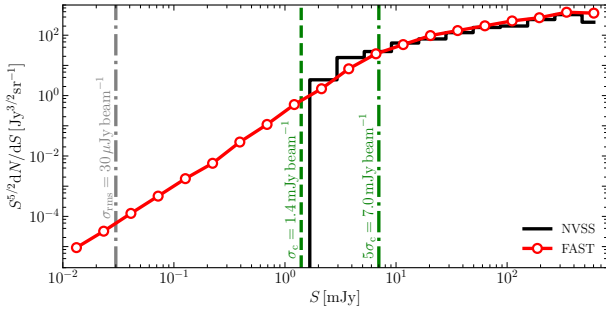


Figure 22. The differential number count of the continuum sources in the survey area. The black stepping curves display the differential number count of the NVSS catalog, while the red circle markers with solid lines display the results of our map. The green vertical dash-dot line indicates the flux limit of $5\sigma_c \approx 7 \text{ mJy beam}^{-1}$, where σ_c , shown with the green vertical dashed line, is the confusion limit due to the background unresolved sources. The gray vertical dashed line indicates the $30 \mu\text{Jy beam}^{-1}$ flux limit of the map.

of the intrinsic spectrum variation of the source that can not be well-fitted by a low-order polynomial function.

4.4. Flux of detected sources

According to the measurements in Section 4.2, in our survey the pixel noise level is $\sim 25.9 \text{ mK}$ with the frequency resolution of 28 kHz at high-frequency band. The corresponding flux limit at 1400 MHz with a bandwidth of 50 MHz should be $\sim 30 \mu\text{Jy beam}^{-1}$. We apply a source finding algorithm, i.e. the DAOS_tFinder⁴, to our map with the threshold of $30 \mu\text{Jy beam}^{-1}$ and aperture size of 3 arcmin and

more than three thousand continuum sources are detected. The flux-weighted differential number count of the detected continuum sources is shown using the red circle markers with the solid curve in Figure 22.

However, we should also consider the confusion limit for the continuum sources (Condon 1974; Meyers et al. 2017),

$$\sigma_c \approx 0.2 \left(\frac{\nu}{\text{GHz}} \right)^{-0.7} \left(\frac{\theta_{\text{FWHM}}}{\text{arcmin}} \right)^2 \approx 1.4 \text{ mJy beam}^{-1}. \quad (42)$$

This is much larger than the limit given above. Sources fainter than a few σ_c would be confused and not detected as individual sources.

To check our survey results, we compare the continuum flux density of the sources in the observed field with those in the NRAO-VLA Sky Survey (NVSS) catalog (Kimball & Ivezić 2008). We use the integrated flux density of NVSS sources from a combined radio objects catalog with flux and position corrections⁵. The flux limit of the NVSS catalog is given as 2 mJy beam^{-1} . There are 3161 NVSS sources in the survey area, i.e. $9^{\text{h}} < \text{R.A.} < 13^{\text{h}}$ and $+25^{\circ}83' < \text{Dec} < +27^{\circ}08'$. The flux-weighted differential number count for sources in the NVSS catalog is also shown in Figure 22 with the black stepping curves. The detected continuum sources using our map is consistent with the NVSS down to $\sim 7 \text{ mJy beam}^{-1} \approx 5\sigma_c$. At the faint end below 7 mJy (marked in the figure by the vertical dash-dot line), the number of sources detected by our survey begins to fall below that of the NVSS, which is unsurprising because the NVSS has much higher angular resolution and therefore lower the confusion limit.

⁴ <https://photutils.readthedocs.io/en/stable/api/photutils.detection.DAOSFinder.html>

⁵ <http://www.aoc.nrao.edu/~akimball/radiocat.shtml>

Table 2. Bright sources used for bandpass shape inspection. The flux values are all in the unit of mJy

Source name	74 MHz ^a	151 MHz ^b	365 MHz ^c	408 MHz ^d	1400 MHz ^e	4850 MHz ^f
B2 1010+27A	1440 ± 170	910 ± 66	424 ± 26	470 ± 72	158 ± 4.8	40 ± 6.0
B2 1016+26	–	700 ± 63	357 ± 25	304 ± 70	121 ± 4.3	39 ± 5.9
B2 1018+26	1660 ± 190	1400 ± 79	640 ± 57	735 ± 80	228 ± 7.7	76 ± 11
B2 1036+26	1180 ± 140	870 ± 59	–	354 ± 70	145 ± 4.7	46 ± 6.9
B2 1037+26	1840 ± 260	860 ± 63	408 ± 32	425 ± 72	124 ± 4.4	30 ± 7.0
B2 1039+27	1880 ± 200	1200 ± 66	559 ± 30	603 ± 72	149 ± 4.5	31 ± 4.7
B2 1054+26	4620 ± 490	2650 ± 133	1520 ± 53	1260 ± 100	436 ± 15	95 ± 14
B2 1138+27	2150 ± 230	1380 ± 97	816 ± 26	873 ± 80	284 ± 8.5	92 ± 14
B2 1202+26	2250 ± 240	2110 ± 124	1250 ± 172	969 ± 80	379 ± 11	141 ± 21
B2 1203+26B	770 ± 130	670 ± 98	415 ± 38	420 ± 72	156 ± 4.7	63 ± 9.5

^a The VLA Low-Frequency Sky Survey (Cohen et al. 2007).

^b The 7C survey of radio sources at 151 MHz (Waldram et al. 1996).

^c The Texas Survey of Radio Sources (Douglas et al. 1996)

^d The B2 Catalogue of radio sources (Colla et al. 1972).

^e The NRAO VLA Sky Survey (Condon et al. 1998).

^f A New Catalog of 53522 4.85 GHz Sources (Becker et al. 1991).

In order to make source-by-source flux measurement comparison, we select isolated bright sources from the full NVSS sample according to the following criteria:

- i) We reject the sources that have neighbors' flux over 10% of the centra source within 9 arcmin, i.e. about three times of the beam width (Gregory et al. 1996). Such selection criteria reject more than 90% of the NVSS sources in the field.
- ii) Then we remove the sources with flux less than 14 mJy beam⁻¹. We adopt such an aggressive flux limit to avoid confusion from the background noise. Another 3% source is rejected according to this criteria.
- iii) In the end, we pick the closely scanned sources that are $0.5\theta_{\text{FWHM}} \sim 1.5$ arcmin or less from the center of at least one FAST beam.

A total of 81 isolated sources meet these selection criteria, making up the isolated sample. This sample is listed in Table 3. This isolated sample of sources is used for the following source-by-source flux measurement comparison.

4.4.1. Flux comparison with time-ordered data

We first make a comparison of flux from the TOD. We use the mean flux density across the frequency range 1.375 ~ 1.425 GHz, which is the same frequency range of the NVSS catalog (Condon et al. 1998). Because the sky coverage partially overlaps between different days, the same source may be observed by different beams on different days. The number of sources used for each feed is listed below,

Feed #	01	02	03	04	05	06	07	08	09	10
N	19	24	17	23	9	15	18	18	12	5
Feed #	11	12	13	14	15	16	17	18	19	
N	19	8	20	19	23	15	10	23	10	

The measured flux density is extracted by taking the spectrum density at the time when the source has the minimal angular distance to the feed center, and is compared with the expected flux, which is obtained by multiplying The NVSS flux density with a Gaussian beam profile according to the angular distance to the beam center,

$$\hat{S}_{\text{NVSS}} = S_{\text{NVSS}} \exp \left[-\frac{1}{2} \frac{\theta_{\text{min}}^2}{\left(\theta_{\text{FWHM}} / (2\sqrt{2 \ln 2}) \right)^2} \right]. \quad (43)$$

The flux-flux comparison is plotted in Figure 23. The NVSS sources scanned by different feeds are shown with different colors and those sources scanned by the central, inner circle, and outer circle of the FAST feed arrays are shown in the top, middle, and bottom sub-panels, respectively. The measured flux densities are shown to be consistent with the NVSS catalog.

We quantified the scattering of the measurements using the relative flux residual with respect to the total flux,

$$\delta S = \left(S - \hat{S}_{\text{NVSS}} \right) / \sqrt{S \hat{S}_{\text{NVSS}}}, \quad (44)$$

where S represents the extracted fluxes from our TOD. The histogram statistic of the flux residuals is illustrated in Figure 24. The sources scanned by different feeds are also shown with different colors and those sources scanned with the feeds in the central, the inner circle and the outer circle of the feed

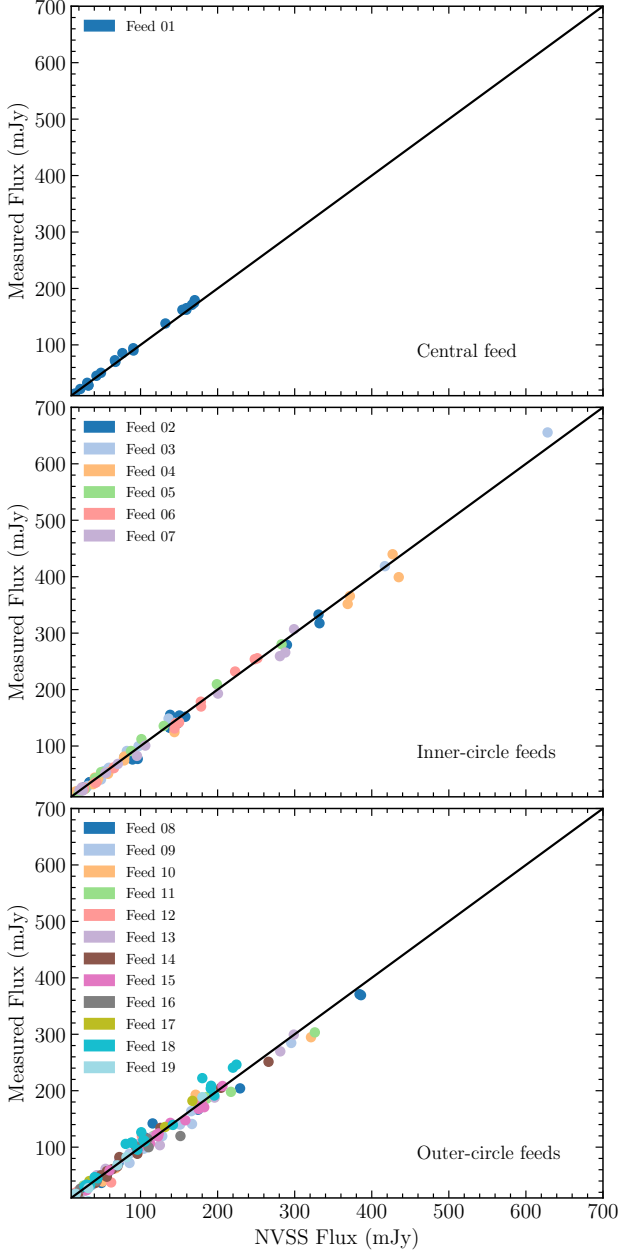


Figure 23. The flux-flux diagram compares the measurements using the TOD with those in the NVSS catalog.

array is shown in the top, middle, and bottom sub-panels, respectively. The black solid curves show the averaged histogram of the feed categories. All the histograms are normalized with the total number of measurements. The rms of the relative flux residual, i.e. $\sqrt{\sum \delta S^2 / N_{\text{total}}} \times 100\%$, of the three feed categories are 4.2%, 5.3% and 6.9%, respectively. The source flux measured with the central feed has less scattering than measurements with the rest of the feeds. The increasing residue for feeds in the inner and outer circle of the feed array is probably a result of an error in the beam model, as the beams are more distorted as we move out from the center.

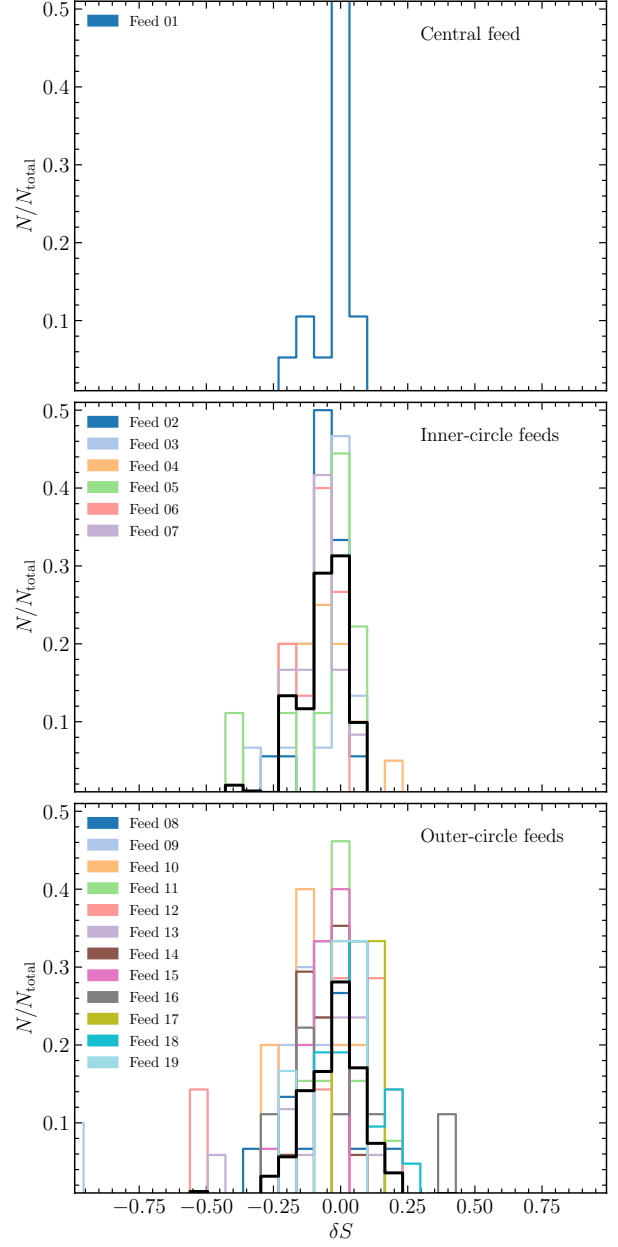


Figure 24. The histogram of relative flux residual between our measurements using the TOD and the NVSS catalog, i.e. Equation (44).

We also check the flux measurements uncertainty between the observation on different days. The results show that the flux residual rms of different days are generally consistent. We can also take advantage of the repeated observation of the same strip on March 9th, 2021, and March 14th, 2021. We estimate the relative residual rms using the flux differences of the same sources between these two observations.

$$\sqrt{\sum \delta S_{ab}^2 / N_{\text{total}} / 2} \times 100\% = 3.7\%,$$

where $\delta S_{ab} = (S_a - S_b) / \sqrt{S_a S_b}$ is the flux difference. As the observations on such two days have the same pointing direc-

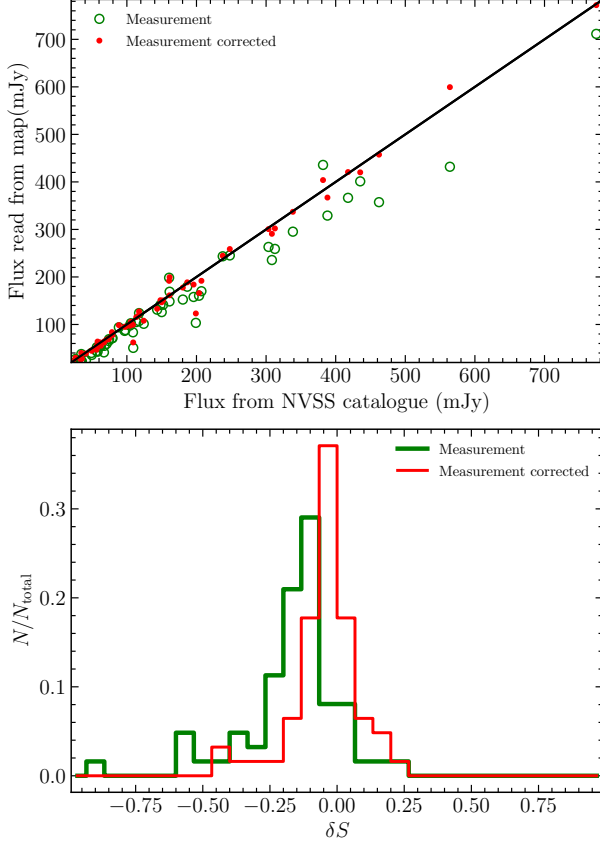


Figure 25. Map-domain flux measurements comparing. The flux measurements before and after correction with simulation are shown in green and red, respectively. Top panel: the x-axis is the flux values from the NVSS catalog and the y-axis is the flux measurements from the map; Bottom-panel: the histogram statistic of the relative flux residual, i.e. Equation (44). All the measurements use an aperture radius size of 1.5 arcmin.

tion, the systematic effect, such as the beam effect, is canceled. If the source flux variation between the short period is negligible, such relative residual rms indicates the calibration uncertainties in our point source flux measurements. The residual between these two observations is significantly less than the residual between our measurements and the NVSS catalog. The additional discrepancies between our results and the NVSS database could result from a number of different factors. For instance, a less accurate beam model or the flux variation of the NVSS source. Thus, the $\sim 6.3\%$ flux dispersion on average indicates an upper bound on the residual gain variations after the calibration process.

4.4.2. Flux comparison with the combined map

Next, we make the flux density comparison using a map with a fine angular resolution created using the map-making process, as described in Haynes et al. (2018). We average the flux density of pixels within an aperture radius of $0.5\theta_{\text{FWHM}} \sim$

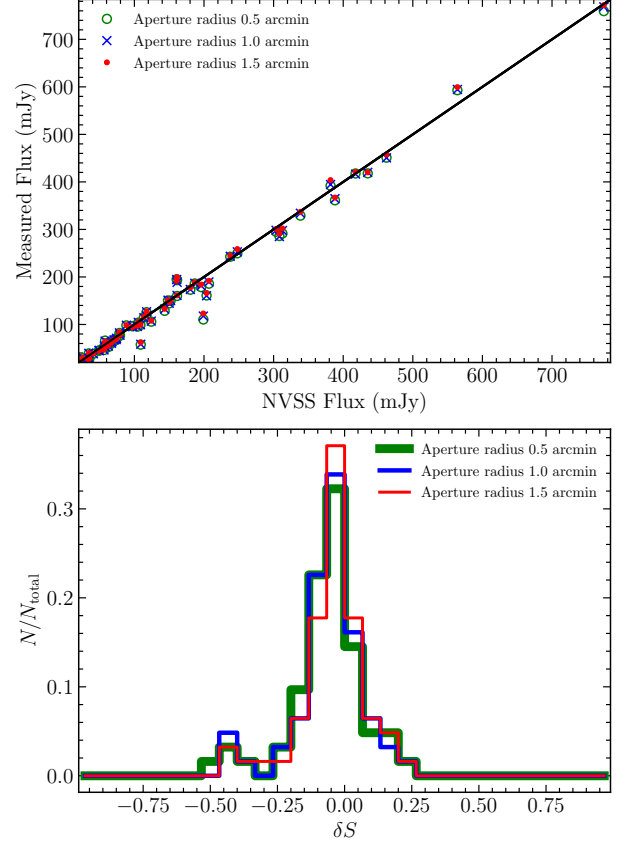


Figure 26. Map-domain flux measurements with different aperture radius sizes. Top panel: the x-axis is the flux values from the NVSS catalog and the y-axis is the flux measurements from the map; Bottom-panel: the histogram statistic of the relative flux residual, i.e. Equation (44).

1.5 arcmin via (Fabello et al. 2011)

$$S = \frac{\sum_i S(\theta_i)}{\sum_i K'(\theta_i)}, \quad \sigma_S^2 = \frac{\sum_i K'^2(\theta_i)}{(\sum_i K'(\theta_i))^2} \frac{\sum_i (S(\theta_i) - K'S)^2}{\sum_i K'^2(\theta_i)}, \quad (45)$$

where σ_S is the measurements error, θ_i is the angular separation to the center pixel and $K'(\theta_i)$ represents the kernel function used in the map domain,

$$K'(\theta_i) = \exp\left[-\frac{1}{2}\left(\frac{\theta_i}{\sigma_{K'}}\right)^2\right], \quad (46)$$

where $\sigma_{K'} = \sigma_K + \theta_{\text{FWHM}}/(2\sqrt{2\ln 2})$, σ_K is the kernel size of Equation (36) that applied during the map-making and θ_{FWHM} is the beam size. We use the same NVSS sources selected in Section 4.4.1 for comparison.

However, a direct comparison of bright pixels in the map with the NVSS source flux would show a large bias. This is because the sources do not always transit across the beam center, but in the map-making process no correction has been

made, as we can not presume that we know the sources and their positions. With a sufficiently large number of scans, the sources would be completely sampled, and the flux measurements taken after constructing the maps would be unbiased. However, due to the limited number of scans, and also RFI flagging, noise diode injection, and abandoning of data from bad beams, the sources are far from completely sampled. In order to recover the bias raises from the incomplete sampling of the sources, we simulate the TOD using the NVSS catalog. The simulated TOD has the same sky coordinates and mask as the real data and is projected to the map domain using the same map-making procedure as observations. We discover that the flux from most sources is pretty biased. The map-domain flux values are then corrected using the difference between the flux from the simulation and the NVSS catalog. The comparison of the flux before and after correction is shown in Figure 25. The top panel shows the flux-flux comparison between map-domain measurements and the NVSS catalog and the bottom panel show the histogram statistic of the relative flux residual defined in Equation (44). It is obvious that the measurements are significantly biased in the absence of flux correction. The flux correction makes a significant improvement, i.e. the measurement's relative uncertainty is improved from 17.1% to 6.3% after the flux correction.

We also investigate how aperture size affects flux measurements. We vary the aperture radius size between 0.5 arcmin, 1.0 arcmin and 1.5 arcmin and show the comparison results in Figure 26. All the measurements are corrected using the simulation with the corresponding aperture size. With varying aperture radius sizes, the flux values only slightly varied without a clear systematic trend.

The map-domain flux measurements result in about 6.3% relative uncertainty, which is consistent with the uncertainty of the TOD flux measurements. It shows that our map-making procedure is accurate enough for continuum flux measurements. For the flux check in this work, we only selected a small number of bright, isolated point sources. We leave the work of identifying weak and diffuse sources to future studies.

5. SUMMARY

The neutral hydrogen (HI) is known to trace the galaxies in the post-reionization era. A comprehensive wide-field of the extragalactic HI survey could provide valuable information for both cosmology and astrophysics research. In this work, we report the time-ordered data (TOD) analysis pipeline designed for drift-scan observation using the Five-hundred-meter Aperture Spherical Telescope (FAST).

The data analyzed in this work were collected over a few nights spanning in 2019, 2020, and 2021. During the 4 hours drift scan of each night, the FAST telescope points at a fixed altitude angle and the observation covers right ascension (R. A.) range from 9 hr to 13 hr, which overlaps with the Northern

Galactic Cap (NGP) area of the Sloan Digital Sky Survey (SDSS). The FAST L-band 19-feed receiver is used in our observation. The feed array is rotated by $23^{\circ}4'$ to optimize the coverage. The pointing Dec. shift by 10.835 arcmin between different days to enlarge the survey area.

The noise diode signal, as the relative calibrator, is injected for 1 s in every 8 s. The noise diode signal is used for calibrating the bandpass gain and temporal drift of the gain. Our analysis indicates that the observation data in 2019 have significant bandpass shape variation during the 4 hours drift-scan observation. The bandpass shape of the data in 2021 becomes much more stable. The major data analysis focuses on the 7 nights observations in 2021.

We applied the `SumThreshold` and `SIR` radio frequency interference (RFI) flagging program to the bandpass calibrated data. In order to enhance the RFI signal and protect the potentially existing HI emission lines, the RFI flagging is applied to the feed averaged data. Due to the contamination of the Global Navigation Satellite Systems, the data between the frequency range of 1135-1310 MHz are mostly flagged. Besides, about 40% and 14% data are flagged in the frequency range of 1050-1135 MHz (the low-frequency band) and 1310-1450 MHz (the high-frequency band), respectively.

We develop the temporal drift calibration strategy that estimates the gain variation across the drift-scan observation by applying a Wiener filter on the gain variation measurements. The Wiener filter is designed according to the $1/f$ noise temporal power spectrum model, which is constrained using the observation data. With our calibration strategy, a temporal oscillation of the gain is observed in the 4 hours drift scan and such oscillation can be well calibrated.

The absolute flux calibration is done by calibrating the noise diode spectrum against the celestial source 3C286. The calibration observation is made also in drift scan mode. The noise diode spectrum shape is stable during the 7 nights observations in 2021. Besides, using the drift scan observation of bright source 3C286, we check the beam profile for each of the feeds. The beam profiles of all the 19 feeds are significantly asymmetric.

Due to the systematic background noise level variation during the observation time, a significant temporal baseline variation is observed with the gain-calibrated data. Especially, some sharp variations are shown in one night of the observations. Such baseline variations are subtracted by fitting with a baseline template, which is constructed using the baseline averaged across different feeds. After baseline subtraction, the calibrated data are zero-centered and transferred to the standard map-making procedure.

We check the standing-wave ripples across the frequency axis by estimating the delay spectrum using well-calibrated data. The standing-wave signature is more prominent in the bandpass measurements than in the sky observation, probably

because this standing wave is induced by the noise diode. We use the low-pass filter with the size of $\tau_c = 0.7 \mu s$ to suppress both the noise and standing-wave signature during the band-pass determination. The standing-wave peak is negligible during our observations.

We check the measurement noise level using the TOD following the method introduced in Wang et al. (2021). The noise level of the low- and high-frequency bands are 116.39 mK and 99.47 mK, respectively. The noise level also varies between different feeds. The feed in the outer circle of the feed array has a noise level increasing more than 10% than the central feed. The noise level reduces slowly after integrating the measurements via map-making, due to weak RFI contamination, residual sky emission, or correlated noise.

We also study the systematic uncertainties by comparing the continuum flux measurements with the NVSS catalog. By applying the source-finding algorithm with the threshold of $30 \mu Jy beam^{-1}$, i.e. the flux limit due to the map rms, more than three thousand continuum sources are detected within our survey field. However, most of them are confused sources due to the angular resolution limit of the FAST beam. The flux-weighted differential number counts for the detected sources are consistent with the NVSS catalog down to $\sim 7 mJy beam^{-1}$, which is about 5 times of the confusion limit. Finally, we chose 81 isolated NVSS sources

with flux over $14 mJy beam^{-1}$ in our survey field and find that the calibrated data shows about 4.2%, 5.3% and 6.9% measurement uncertainties for the central feed, inner circle feeds and outer circle feeds, respectively. Such uncertainty varies between the measurements of central feed, inner-circle feeds, and outer-circle feeds. Finally, there is about 6.3% uncertainty on average, which is consistent with the map-domain flux measurements.

ACKNOWLEDGEMENTS

This work made use of the data from FAST (Five-hundred-meter Aperture Spherical radio Telescope). FAST is a Chinese national mega-science facility, operated by National Astronomical Observatories, Chinese Academy of Sciences. We acknowledge the support of the National SKA Program of China (Nos. 2022SKA0110100, 2022SKA0110200, 2022SKA0110203), the National Natural Science Foundation of China (Nos. 11975072, 11835009), the CAS Interdisciplinary Innovation Team (JCTD-2019-05), and the science research grants from the China Manned Space Project with No. CMS-CSST-2021-B01. LW is a UK Research and Innovation Future Leaders Fellow [grant MR/V026437/1].

DATA AVAILABILITY

The data underlying this article will be shared on reasonable request to the corresponding author.

REFERENCES

- Anderson, C. J., Luciw, N. J., Li, Y. C., et al. 2018, *Monthly Notices of the Royal Astronomical Society*, 476, 3382, doi: [10.1093/mnras/sty346](https://doi.org/10.1093/mnras/sty346)
- Anderson, L., Aubourg, É., Bailey, S., et al. 2014, *Monthly Notices of the Royal Astronomical Society*, 441, 24, doi: [10.1093/mnras/stu523](https://doi.org/10.1093/mnras/stu523)
- Ansari, R., Campagne, J. E., Colom, P., et al. 2012, *Astronomy and Astrophysics*, 540, A129, doi: [10.1051/0004-6361/201117837](https://doi.org/10.1051/0004-6361/201117837)
- Bagla, J. S., Khandai, N., & Datta, K. K. 2010, *Monthly Notices of the Royal Astronomical Society*, 407, 567, doi: [10.1111/j.1365-2966.2010.16933.x](https://doi.org/10.1111/j.1365-2966.2010.16933.x)
- Bandura, K., Addison, G. E., Amiri, M., et al. 2014, *Society of Photo-Optical Instrumentation Engineers (SPIE) Conference Series*, Vol. 9145, Canadian Hydrogen Intensity Mapping Experiment (CHIME) pathfinder, 914522, doi: [10.1117/12.2054950](https://doi.org/10.1117/12.2054950)
- Barnes, D. G., Staveley-Smith, L., de Blok, W. J. G., et al. 2001, *Monthly Notices of the Royal Astronomical Society*, 322, 486, doi: [10.1046/j.1365-8711.2001.04102.x](https://doi.org/10.1046/j.1365-8711.2001.04102.x)
- Battye, R. A., Browne, I. W. A., Dickinson, C., et al. 2013, *Monthly Notices of the Royal Astronomical Society*, 434, 1239, doi: [10.1093/mnras/stt1082](https://doi.org/10.1093/mnras/stt1082)
- Battye, R. A., Davies, R. D., & Weller, J. 2004, *Monthly Notices of the Royal Astronomical Society*, 355, 1339, doi: [10.1111/j.1365-2966.2004.08416.x](https://doi.org/10.1111/j.1365-2966.2004.08416.x)
- Becker, R. H., White, R. L., & Edwards, A. L. 1991, *The Astrophysical Journal Supplement Series*, 75, 1, doi: [10.1086/191529](https://doi.org/10.1086/191529)
- Bull, P., Ferreira, P. G., Patel, P., & Santos, M. G. 2015, *The Astrophysical Journal*, 803, 21, doi: [10.1088/0004-637X/803/1/21](https://doi.org/10.1088/0004-637X/803/1/21)
- Chang, T.-C., Pen, U.-L., Bandura, K., & Peterson, J. B. 2010, *Nature*, 466, 463, doi: [10.1038/nature09187](https://doi.org/10.1038/nature09187)
- Chang, T.-C., Pen, U.-L., Peterson, J. B., & McDonald, P. 2008, *Physical Review Letter*, 100, 091303, doi: [10.1103/PhysRevLett.100.091303](https://doi.org/10.1103/PhysRevLett.100.091303)
- Chen, X. 2012, in *International Journal of Modern Physics Conference Series*, Vol. 12, International Journal of Modern Physics Conference Series, 256–263, doi: [10.1142/S2010194512006459](https://doi.org/10.1142/S2010194512006459)
- Chen, Z., Chapman, E., Wolz, L., & Mazumder, A. 2023, arXiv e-prints, arXiv:2302.11504, doi: [10.48550/arXiv.2302.11504](https://doi.org/10.48550/arXiv.2302.11504)
- CHIME Collaboration, Amiri, M., Bandura, K., et al. 2022, arXiv e-prints, arXiv:2202.01242, doi: [10.48550/arXiv.2202.01242](https://doi.org/10.48550/arXiv.2202.01242)

- Cohen, A. S., Lane, W. M., Cotton, W. D., et al. 2007, *The Astronomical Journal*, 134, 1245, doi: [10.1086/520719](https://doi.org/10.1086/520719)
- Cole, S., Percival, W. J., Peacock, J. A., et al. 2005, *Monthly Notices of the Royal Astronomical Society*, 362, 505, doi: [10.1111/j.1365-2966.2005.09318.x](https://doi.org/10.1111/j.1365-2966.2005.09318.x)
- Colla, G., Fanti, C., Fanti, R., et al. 1972, *A&AS*, 7, 1
- Condon, J. J. 1974, *The Astrophysical Journal*, 188, 279, doi: [10.1086/152714](https://doi.org/10.1086/152714)
- Condon, J. J., Cotton, W. D., Greisen, E. W., et al. 1998, *The Astronomical Journal*, 115, 1693, doi: [10.1086/300337](https://doi.org/10.1086/300337)
- Cunnington, S., Li, Y., Santos, M. G., et al. 2022, arXiv e-prints, arXiv:2206.01579. <https://arxiv.org/abs/2206.01579>
- Douglas, J. N., Bash, F. N., Bozyan, F. A., Torrence, G. W., & Wolfe, C. 1996, *The Astronomical Journal*, 111, 1945, doi: [10.1086/117932](https://doi.org/10.1086/117932)
- eBOSS Collaboration, Alam, S., Aubert, M., et al. 2020, arXiv e-prints, arXiv:2007.08991. <https://arxiv.org/abs/2007.08991>
- Eisenstein, D. J., Zehavi, I., Hogg, D. W., et al. 2005, *The Astrophysical Journal*, 633, 560, doi: [10.1086/466512](https://doi.org/10.1086/466512)
- Fabello, S., Catinella, B., Giovanelli, R., et al. 2011, *Monthly Notices of the Royal Astronomical Society*, 411, 993, doi: [10.1111/j.1365-2966.2010.17742.x](https://doi.org/10.1111/j.1365-2966.2010.17742.x)
- Giovanelli, R., Haynes, M. P., Kent, B. R., et al. 2005, *The Astronomical Journal*, 130, 2598, doi: [10.1086/497431](https://doi.org/10.1086/497431)
- . 2007, *The Astronomical Journal*, 133, 2569, doi: [10.1086/516635](https://doi.org/10.1086/516635)
- Gregory, P. C., Scott, W. K., Douglas, K., & Condon, J. J. 1996, *The Astrophysical Journal Supplement Series*, 103, 427, doi: [10.1086/192282](https://doi.org/10.1086/192282)
- Harper, S. E., Dickinson, C., Battye, R. A., et al. 2018, *Monthly Notices of the Royal Astronomical Society*, 478, 2416, doi: [10.1093/mnras/sty1238](https://doi.org/10.1093/mnras/sty1238)
- Haynes, M. P., Giovanelli, R., Kent, B. R., et al. 2018, *The Astrophysical Journal*, 861, 49, doi: [10.3847/1538-4357/aac956](https://doi.org/10.3847/1538-4357/aac956)
- Hinton, S. R., Kazin, E., Davis, T. M., et al. 2017, *Monthly Notices of the Royal Astronomical Society*, 464, 4807, doi: [10.1093/mnras/stw2725](https://doi.org/10.1093/mnras/stw2725)
- Hu, W., Wang, X., Wu, F., et al. 2020, *Monthly Notices of the Royal Astronomical Society*, 493, 5854, doi: [10.1093/mnras/staa650](https://doi.org/10.1093/mnras/staa650)
- Hu, W., Li, Y., Wang, Y., et al. 2021, *Monthly Notices of the Royal Astronomical Society*, 508, 2897, doi: [10.1093/mnras/stab2728](https://doi.org/10.1093/mnras/stab2728)
- Jarvis, M. J., Bhatnagar, S., Bruggen, M., et al. 2014, arXiv e-prints, arXiv:1401.4018. <https://arxiv.org/abs/1401.4018>
- Jiang, P., Tang, N.-Y., Hou, L.-G., et al. 2020, *Research in Astronomy and Astrophysics*, 20, 064, doi: [10.1088/1674-4527/20/5/64](https://doi.org/10.1088/1674-4527/20/5/64)
- Jin, S.-J., Wang, L.-F., Wu, P.-J., Zhang, J.-F., & Zhang, X. 2021, *Phys. Rev. D*, 104, 103507, doi: [10.1103/PhysRevD.104.103507](https://doi.org/10.1103/PhysRevD.104.103507)
- Kimball, A. E., & Ivezić, Ž. 2008, *The Astronomical Journal*, 136, 684, doi: [10.1088/0004-6256/136/2/684](https://doi.org/10.1088/0004-6256/136/2/684)
- Lang, R. H., Boyce, P. J., Kilborn, V. A., et al. 2003, *Monthly Notices of the Royal Astronomical Society*, 342, 738, doi: [10.1046/j.1365-8711.2003.06535.x](https://doi.org/10.1046/j.1365-8711.2003.06535.x)
- Li, D., & Pan, Z. 2016, *Radio Science*, 51, 1060, doi: [10.1002/2015RS005877](https://doi.org/10.1002/2015RS005877)
- Li, D., Wang, P., Qian, L., et al. 2018, *IEEE Microwave Magazine*, 19, 112, doi: [10.1109/MMM.2018.2802178](https://doi.org/10.1109/MMM.2018.2802178)
- Li, J., Zuo, S., Wu, F., et al. 2020, *Science China Physics, Mechanics, and Astronomy*, 63, 129862, doi: [10.1007/s11433-020-1594-8](https://doi.org/10.1007/s11433-020-1594-8)
- Li, Y., Santos, M. G., Grainge, K., Harper, S., & Wang, J. 2021, *Monthly Notices of the Royal Astronomical Society*, 501, 4344, doi: [10.1093/mnras/staa3856](https://doi.org/10.1093/mnras/staa3856)
- Li, Y.-C., & Ma, Y.-Z. 2017, *Physical Review D*, 96, 063525, doi: [10.1103/PhysRevD.96.063525](https://doi.org/10.1103/PhysRevD.96.063525)
- Lidz, A., Furlanetto, S. R., Oh, S. P., et al. 2011, *The Astrophysical Journal*, 741, 70, doi: [10.1088/0004-637X/741/2/70](https://doi.org/10.1088/0004-637X/741/2/70)
- Loeb, A., & Wyithe, J. S. B. 2008, *Physical Review Letter*, 100, 161301, doi: [10.1103/PhysRevLett.100.161301](https://doi.org/10.1103/PhysRevLett.100.161301)
- Mao, Y., Tegmark, M., McQuinn, M., Zaldarriaga, M., & Zahn, O. 2008, *Physical Review D*, 78, 023529, doi: [10.1103/PhysRevD.78.023529](https://doi.org/10.1103/PhysRevD.78.023529)
- Masui, K. W., Switzer, E. R., Banavar, N., et al. 2013, *Astrophysical Journal Letters*, 763, L20, doi: [10.1088/2041-8205/763/1/L20](https://doi.org/10.1088/2041-8205/763/1/L20)
- Matshawule, S. D., Spinelli, M., Santos, M. G., & Ngobese, S. 2020, arXiv e-prints, arXiv:2011.10815. <https://arxiv.org/abs/2011.10815>
- McQuinn, M., Zahn, O., Zaldarriaga, M., Hernquist, L., & Furlanetto, S. R. 2006, *The Astrophysical Journal*, 653, 815, doi: [10.1086/505167](https://doi.org/10.1086/505167)
- Meyer, M. J., Zwaan, M. A., Webster, R. L., et al. 2004, *Monthly Notices of the Royal Astronomical Society*, 350, 1195, doi: [10.1111/j.1365-2966.2004.07710.x](https://doi.org/10.1111/j.1365-2966.2004.07710.x)
- Meyers, B. W., Hurley-Walker, N., Hancock, P. J., et al. 2017, *Publications Astronomical Society of Australia*, 34, e013, doi: [10.1017/pasa.2017.5](https://doi.org/10.1017/pasa.2017.5)
- Nan, R., Li, D., Jin, C., et al. 2011, *International Journal of Modern Physics D*, 20, 989, doi: [10.1142/S0218271811019335](https://doi.org/10.1142/S0218271811019335)
- Newburgh, L. B., Bandura, K., Bucher, M. A., et al. 2016, *Society of Photo-Optical Instrumentation Engineers (SPIE) Conference Series*, Vol. 9906, HIRAX: a probe of dark energy and radio transients, 99065X, doi: [10.1117/12.2234286](https://doi.org/10.1117/12.2234286)
- Offringa, A. R., de Bruyn, A. G., Biehl, M., et al. 2010, *Monthly Notices of the Royal Astronomical Society*, 405, 155, doi: [10.1111/j.1365-2966.2010.16471.x](https://doi.org/10.1111/j.1365-2966.2010.16471.x)
- Offringa, A. R., van de Gronde, J. J., & Roerdink, J. B. T. M. 2012, *Astronomy and Astrophysics*, 539, A95, doi: [10.1051/0004-6361/201118497](https://doi.org/10.1051/0004-6361/201118497)

- Paul, S., Santos, M. G., Chen, Z., & Wolz, L. 2023, arXiv e-prints, arXiv:2301.11943, doi: [10.48550/arXiv.2301.11943](https://doi.org/10.48550/arXiv.2301.11943)
- Paul, S., Santos, M. G., Townsend, J., et al. 2021, *Monthly Notices of the Royal Astronomical Society*, 505, 2039, doi: [10.1093/mnras/stab1089](https://doi.org/10.1093/mnras/stab1089)
- Perdereau, O., Ansari, R., Stebbins, A., et al. 2022, *Monthly Notices of the Royal Astronomical Society*, 517, 4637, doi: [10.1093/mnras/stac2832](https://doi.org/10.1093/mnras/stac2832)
- Perley, R. A., & Butler, B. J. 2017, *The Astrophysical Journal Supplement Series*, 230, 7, doi: [10.3847/1538-4365/aa6df9](https://doi.org/10.3847/1538-4365/aa6df9)
- Peterson, J. B., Aleksan, R., Ansari, R., et al. 2009, in *astro2010: The Astronomy and Astrophysics Decadal Survey*, Vol. 2010, 234. <https://arxiv.org/abs/0902.3091>
- Pritchard, J. R., & Loeb, A. 2008, *Physical Review D*, 78, 103511, doi: [10.1103/PhysRevD.78.103511](https://doi.org/10.1103/PhysRevD.78.103511)
- . 2012, *Reports on Progress in Physics*, 75, 086901, doi: [10.1088/0034-4885/75/8/086901](https://doi.org/10.1088/0034-4885/75/8/086901)
- Reid, B., Ho, S., Padmanabhan, N., et al. 2016, *Monthly Notices of the Royal Astronomical Society*, 455, 1553, doi: [10.1093/mnras/stv2382](https://doi.org/10.1093/mnras/stv2382)
- Saintonge, A. 2007, *The Astronomical Journal*, 133, 2087, doi: [10.1086/513515](https://doi.org/10.1086/513515)
- Santos, M., Bull, P., Alonso, D., et al. 2015, in *Advancing Astrophysics with the Square Kilometre Array (AASKA14)*, 19. <https://arxiv.org/abs/1501.03989>
- Santos, M. G., Cluver, M., Hilton, M., et al. 2017, arXiv e-prints, arXiv:1709.06099. <https://arxiv.org/abs/1709.06099>
- Seo, H.-J., Dodelson, S., Marriner, J., et al. 2010, *The Astrophysical Journal*, 721, 164, doi: [10.1088/0004-637X/721/1/164](https://doi.org/10.1088/0004-637X/721/1/164)
- Square Kilometre Array Cosmology Science Working Group, Bacon, D. J., Battye, R. A., et al. 2020, *Publications Astronomical Society of Australia*, 37, e007, doi: [10.1017/pasa.2019.51](https://doi.org/10.1017/pasa.2019.51)
- Sun, S., Li, J., Wu, F., et al. 2022, *Research in Astronomy and Astrophysics*, 22, 065020, doi: [10.1088/1674-4527/ac684d](https://doi.org/10.1088/1674-4527/ac684d)
- Switzer, E. R., Masui, K. W., Bandura, K., et al. 2013, *Monthly Notices of the Royal Astronomical Society*, 434, L46, doi: [10.1093/mnras/slt074](https://doi.org/10.1093/mnras/slt074)
- Tegmark, M. 1997, *Astrophysical Journal Letters*, 480, L87, doi: [10.1086/310631](https://doi.org/10.1086/310631)
- Teunissen, P. J., & Montenbruck, O. 2017, *Handbook of Global Navigation Satellite Systems*, doi: [10.1007/978-3-319-42928-1](https://doi.org/10.1007/978-3-319-42928-1)
- Waldram, E. M., Yates, J. A., Riley, J. M., & Warner, P. J. 1996, *Monthly Notices of the Royal Astronomical Society*, 282, 779, doi: [10.1093/mnras/282.3.779](https://doi.org/10.1093/mnras/282.3.779)
- Wang, J., Santos, M. G., Bull, P., et al. 2021, *Monthly Notices of the Royal Astronomical Society*, 505, 3698, doi: [10.1093/mnras/stab1365](https://doi.org/10.1093/mnras/stab1365)
- Wolz, L., Blake, C., Abdalla, F. B., et al. 2017, *Monthly Notices of the Royal Astronomical Society*, 464, 4938, doi: [10.1093/mnras/stw2556](https://doi.org/10.1093/mnras/stw2556)
- Wolz, L., Pourtsidou, A., Masui, K. W., et al. 2022, *Monthly Notices of the Royal Astronomical Society*, 510, 3495, doi: [10.1093/mnras/stab3621](https://doi.org/10.1093/mnras/stab3621)
- Wu, F., Li, J., Zuo, S., et al. 2021, *Monthly Notices of the Royal Astronomical Society*, 506, 3455, doi: [10.1093/mnras/stab1802](https://doi.org/10.1093/mnras/stab1802)
- Wu, P.-J., Li, Y., Zhang, J.-F., & Zhang, X. 2022a. <https://arxiv.org/abs/2212.07681>
- Wu, P.-J., Shao, Y., Jin, S.-J., & Zhang, X. 2022b. <https://arxiv.org/abs/2202.09726>
- Wu, P.-J., & Zhang, X. 2022, *JCAP*, 01, 060, doi: [10.1088/1475-7516/2022/01/060](https://doi.org/10.1088/1475-7516/2022/01/060)
- Wyithe, J. S. B., & Loeb, A. 2008, *Monthly Notices of the Royal Astronomical Society*, 383, 606, doi: [10.1111/j.1365-2966.2007.12568.x](https://doi.org/10.1111/j.1365-2966.2007.12568.x)
- Wyithe, J. S. B., Loeb, A., & Geil, P. M. 2008, *Monthly Notices of the Royal Astronomical Society*, 383, 1195, doi: [10.1111/j.1365-2966.2007.12631.x](https://doi.org/10.1111/j.1365-2966.2007.12631.x)
- Xu, Y., Wang, X., & Chen, X. 2015, *The Astrophysical Journal*, 798, 40, doi: [10.1088/0004-637X/798/1/40](https://doi.org/10.1088/0004-637X/798/1/40)
- Zhang, M., Li, Y., Zhang, J.-F., & Zhang, X. 2023. <https://arxiv.org/abs/2301.04445>
- Zhang, M., Wang, B., Wu, P.-J., et al. 2021, *Astrophys. J.*, 918, 56, doi: [10.3847/1538-4357/ac0ef5](https://doi.org/10.3847/1538-4357/ac0ef5)
- Zuo, S., Li, J., Li, Y., et al. 2021, *Astronomy and Computing*, 34, 100439, doi: [10.1016/j.ascom.2020.100439](https://doi.org/10.1016/j.ascom.2020.100439)
- Zwaan, M. A., Meyer, M. J., Webster, R. L., et al. 2004, *Monthly Notices of the Royal Astronomical Society*, 350, 1210, doi: [10.1111/j.1365-2966.2004.07782.x](https://doi.org/10.1111/j.1365-2966.2004.07782.x)

APPENDIX

A. CONTINUUM SOURCE CATALOGUE

Table 3. The flux density of the 81 isolated continuum sources over 14 mJy beam^{-1} in the survey field. The sources' sky coordinates at the J2000 epoch are presented in the 'RA' and 'Dec' columns; The flux density measurements read from the combined radio objects catalogue (Kimball & Ivezić 2008) are presented in the ' S_{NVSS} ' column; the flux density measurements from this work are presented in the ' S_{FAST} ' column; and the flux correction fraction with respect to ' S_{NVSS} ' are presented in 'corr.' column. The flux measurements use 1.5 arcmin aperture size and are corrected with the simulation.

RA (J2000)	Dec (J2000)	S_{NVSS} [mJy]	S_{FAST} [mJy]	Correction [%]	RA (J2000)	Dec (J2000)	S_{NVSS} [mJy]	S_{FAST} [mJy]	Correction [%]
09h03m11s67	+26°09'40"28	195.87	184.04 ± 3.88	13.35	09h42m36s39	+26°10'15"27	35.09	27.41 ± 0.90	13.08
10h18m07s13	+26°09'42"51	180.38	177.66 ± 3.80	13.99	09h26m00s53	+25°59'53"30	113.56	115.60 ± 2.97	9.24
10h57m23s15	+26°01'30"18	186.74	188.67 ± 4.89	4.92	11h34m02s19	+26°32'24"54	15.62	13.75 ± 0.39	13.94
12h38m23s54	+26°33'46"43	104.30	97.35 ± 3.34	-0.27	12h39m52s76	+26°32'46"57	49.14	45.11 ± 1.52	10.42
12h48m41s35	+26°33'56"48	74.42	70.56 ± 2.54	1.94	10h13m36s86	+26°52'06"67	157.57	139.77 ± 3.66	9.56
10h45m57s36	+26°52'39"93	56.87	46.13 ± 1.41	12.77	10h46m40s38	+26°54'15"73	163.09	155.16 ± 3.46	13.96
09h21m58s57	+26°21'22"60	206.52	211.16 ± 5.83	1.16	10h16m00s82	+26°22'00"12	27.87	23.13 ± 0.81	2.94
10h48m28s59	+26°22'34"89	237.69	244.67 ± 6.13	0.52	10h52m52s26	+26°22'16"24	105.61	105.37 ± 2.62	2.66
09h27m45s09	+26°13'00"51	150.04	146.74 ± 3.36	13.82	10h40m37s59	+26°13'24"81	29.96	25.01 ± 1.14	13.45
10h54m56s64	+26°12'47"26	338.51	337.11 ± 7.16	12.35	12h11m29s70	+26°14'50"20	67.80	64.70 ± 1.25	14.18
09h49m06s44	+26°01'57"71	20.78	11.63 ± 0.87	15.45	12h57m12s52	+26°01'40"62	62.57	55.22 ± 1.23	1.79
09h18m56s17	+26°33'30"99	20.90	18.22 ± 0.82	22.58	10h39m30s97	+26°33'03"88	143.48	133.02 ± 3.53	1.31
10h59m07s98	+26°34'07"50	56.83	55.56 ± 1.47	6.01	12h36m30s59	+26°35'19"78	564.07	599.41 ± 20.89	29.70
11h22m04s96	+26°13'36"73	303.49	300.70 ± 5.84	12.37	10h22m09s14	+26°23'13"70	161.25	161.32 ± 4.29	7.96
10h55m47s35	+26°23'37"82	152.02	150.63 ± 3.38	6.00	12h05m32s86	+26°25'40"65	278.72	268.41 ± 4.18	27.54
11h25m00s85	+26°06'09"32	56.43	46.94 ± 1.60	5.32	12h19m56s37	+26°07'04"07	109.12	62.21 ± 2.72	10.48
12h21m02s00	+26°08'45"74	199.08	123.17 ± 2.70	9.95	09h02m54s70	+25°55'44"83	19.08	21.38 ± 1.02	19.49
09h16m47s38	+25°54'16"05	73.79	68.79 ± 2.34	4.71	09h28m53s21	+25°54'37"90	69.09	68.43 ± 2.45	9.84
09h33m15s67	+25°55'00"69	61.57	62.32 ± 2.06	12.20	09h44m42s33	+25°54'43"55	774.39	771.98 ± 19.53	7.81
09h45m53s28	+25°56'08"37	54.64	55.52 ± 1.17	22.19	11h08m38s99	+25°56'13"45	88.49	98.64 ± 2.68	5.22
09h40m13s47	+26°26'56"68	124.22	107.93 ± 2.82	5.26	12h53m02s00	+26°27'45"97	203.70	166.13 ± 7.02	2.76
09h18m37s49	+26°50'41"10	105.95	103.85 ± 3.05	8.58	10h42m43s59	+26°50'02"25	148.24	151.05 ± 3.48	6.64
12h04m12s95	+26°50'58"95	417.72	420.74 ± 9.65	12.98	12h19m46s58	+26°17'34"40	29.46	17.75 ± 0.92	17.36
12h20m27s95	+26°19'03"54	32.41	17.92 ± 0.28	12.38	09h13m27s12	+26°02'23"13	67.04	61.94 ± 1.10	30.81
09h17m15s57	+26°03'40"53	58.42	49.17 ± 1.41	7.95	09h40m14s71	+26°03'29"91	462.22	457.43 ± 13.37	21.65
09h41m28s66	+26°04'02"56	79.37	77.97 ± 2.18	8.46	10h05m15s06	+26°03'35"99	180.10	165.31 ± 3.55	23.18
10h24m19s44	+26°05'10"71	20.86	18.40 ± 0.50	5.51	12h22m01s84	+26°04'15"09	60.17	32.34 ± 0.98	28.94
09h30m27s63	+25°52'54"26	78.58	83.92 ± 2.25	16.53	09h17m17s69	+26°45'51"73	22.46	21.96 ± 0.73	14.87
10h35m16s54	+26°15'16"45	388.16	367.07 ± 7.47	9.77	12h02m55s33	+26°15'18"79	51.15	39.83 ± 1.00	13.88
11h34m34s12	+26°52'50"95	108.72	99.49 ± 2.50	14.70	09h05m05s60	+26°11'23"24	207.10	191.89 ± 4.47	10.57
10h11m06s75	+26°38'21"01	33.34	27.02 ± 1.47	9.53	10h19m26s26	+26°38'58"41	117.41	119.92 ± 3.15	10.87
10h25m08s32	+26°36'39"24	14.53	8.41 ± 1.04	17.35	10h31m56s02	+26°38'20"94	96.73	95.41 ± 3.55	9.19
10h57m24s93	+26°38'00"02	435.24	420.13 ± 14.35	4.35	11h25m20s26	+26°38'02"07	49.37	40.30 ± 1.67	5.63
09h23m43s10	+26°34'49"94	41.15	38.81 ± 1.30	34.81	12h42m48s21	+25°58'40"76	308.33	290.77 ± 6.32	17.88
11h06m08s35	+25°52'13"04	38.26	39.91 ± 1.97	10.67	11h27m05s77	+25°50'55"17	117.51	127.43 ± 3.32	2.96
12h00m05s07	+26°44'18"34	34.49	40.04 ± 1.21	6.54	10h33m40s04	+26°42'57"77	16.66	16.56 ± 0.57	13.50
10h54m40s25	+26°41'25"69	63.90	59.84 ± 1.59	7.20	10h14m14s85	+25°52'00"01	37.40	30.04 ± 1.06	21.30
09h54m39s79	+26°39'24"55	312.67	302.08 ± 5.82	13.77	10h39m50s71	+27°01'48"14	14.86	14.63 ± 0.73	5.01
12h24m21s36	+27°01'42"20	97.89	95.13 ± 2.15	7.08	09h31m32s80	+26°40'48"18	70.83	68.01 ± 2.04	12.48
11h02m53s30	+27°03'39"38	35.19	28.59 ± 1.19	18.43	12h50m21s97	+27°04'32"95	49.53	44.96 ± 1.43	18.40
09h15m01s99	+27°01'45"69	26.15	30.06 ± 0.49	10.34					